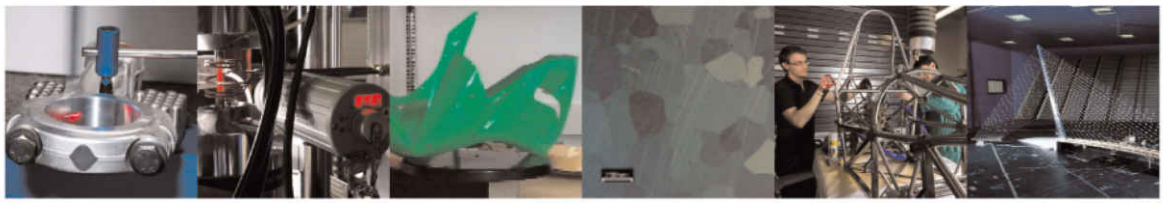

Conformance and nonconformance in segmentation-free X-ray computed tomography geometric inspection

Stefano Petrò, Luca Pagani, Giovanni Moroni, Paul J. Scott

This is a post-peer-review, pre-copyedit version of an article published in Precision Engineering. The final authenticated version is available online at:
http://dx.doi.org/10.1016/j.precisioneng.2021.03.019

DIPARTIMENTO DI MECCANICA ■ POLITECNICO DI MILANO
via G. La Masa, 1 ■ 20156 Milano ■ EMAIL (PEC): pecmecc@cert.polimi.it
http://www.mecc.polimi.it
Rev. 0

Conformance and nonconformance in segmentation-free X-ray computed tomography geometric inspection

Stefano Petrò[a,*], Luca Pagani[b], Giovanni Moroni[a], Paul J. Scott[b]

[a] *Mechanical engineering department, Politecnico di Milano, Via La Masa 1, 20156, Milano, Italy*
[b] *EPSRC Future Metrology Hub, University of Huddersfield, Queensgate, Huddersfield, HD1 3DH, UK*

Abstract

Additive Manufacturing (AM) is changing the manufacturing paradigm as it makes it possible to generate complex geometries that are impossible using conventional technologies. However, conventional GPS/GD&T practices are inadequate both at specifying and verifying geometric tolerances. In both cases, they lack the required flexibility. Applying volumetric instead of surface representations helps to solve the problem of specifying tolerances and coheres with topological optimization. The verification paradigm must be modified, too, as AM allows an increase in part complexity without a corresponding increase of cost. Among measurement techniques, only X-ray computed tomography (XCT), which is volumetric, is capable of easily measure complex parts. Leaving the discussion of volumetric tolerance specifications to the future, the aim of this work is exploring a part geometric accuracy verification by direct comparison between its nominal geometry and geometric tolerance volumetric representation, and an XCT volumetric image of it. Unlike the conventional use of XCT for geometric verification, this is a segmentation-free verification. The method is based on the "mutual information" of the two, i.e. information shared by the measured and nominal representations. The output is a conformance statement that does rely on a measurement but nor on a specific measured value. This

*Correspondig Author. Tel +39 02 23998530. Fax +39 02 23998585.
Email addresses: stefano.petro@polimi.it (Stefano Petrò), L.Pagani@hud.ac.uk (Luca Pagani), giovanni.moroni@polimi.it (Giovanni Moroni)

makes defining a decision rule considering consumer's and producer's risks difficult: uncertainty does not exist in this case. Statistic and simulation techniques make it possible to estimate these risks, defining a numerical model of the distribution of the gray values in a specific portion of the XCT image. Finally, an additive manufacturing case study validates the methodology.

Keywords:
3D X-ray Computed Tomography; Geometric verification; Volumetric representation; Conformance; Decision rule; consumer/customer risk

---

1. Specifications and verification for additive manufacturing parts

The shift of Additive Manufacturing (AM) from prototyping to production has changed mechanical production. Now it is possible to provide "complexity for free" products, i.e. the main cost driver in additive manufacturing is part volume rather than part complexity. However, to take advantage of this novelty, design, production, and verification of AM products still need a significant improvement [1, 2, 3, 4]. Complex geometries, material-process interaction, and internal features are the issues concerning part representation and limiting the current geometric dimensioning and tolerancing/geometric product specification practices [4].

This paper's authors' opinion is that moving from a conventional surface (CAD, mesh, cloud of points, etc.) part representation to a volumetric representation could help to solve these issues. Volumetric representations are representations defining some property(ies) of an object at each coordinate in a three-dimensional space. They are the object representations the closest to simple 2D images, and in fact 3D images is their indication. Volumetric representations cohere to the AM paradigm: filling a volume rather than generating a surface. Deepening the coherence volumetric representations for AM, please consider these propositions. Usually, AM software converts a .stl representation into a part program for the AM machine. However, it is possible to drive an AM machine based on a volumetric representation. Software examples capable

of this are on the market [5]. Besides, topological optimization [6], i.e. by algorithmically optimizing some property of the object (usually lightweightness or stiffness), is often the design basis for parts intended for AM. Topological optimization iteratively adds and removes material from the designed geometry, while verifying coherence with specifications by simulation. This is, of course, coherent with a volumetric representation of parts. Finally, volumetric representations flexibility in representing complex 3D geometries is comparable to 2D images flexibility in representing complex shapes.

The authors of this paper have proposed using an "enriched voxel-based volumetric representation" [1] to describe AM parts. A voxel representation is a volumetric representation constituted by a three-dimensional grid of values. Each point (voxel) of the grid is spatially localized, and a value associated with it quantifies some property. The base idea of enriched voxel-based volumetric representations is to add layers of information to every single voxel. This enables a local specification of the part's properties. Possible information may include, among the others, material, involvement in mating surfaces, deposition layer, presence of support structures. Of course, only a dedicated file format can specify such a representation. Fuji Xerox Co., Ltd [7] is developing such a language.

Among the other properties which are representable by an enriched voxel-based volumetric representation, geometric tolerances coherent with topological optimization are possible. A complete topological optimization returns a "minimum material continuum" (the volume of space that must be material-filled while guaranteeing the part's functionality) and a "maximum material continuum" (the volume of space that can be material-filled without affecting the part's functionality, lightweightness, and cost). These continua define a limit to the geometric variation of the part. An enriched voxel-based volumetric representation can easily specify membership to either continuum.

Specifying tolerances is insufficient. Tolerance verification is mandatory, too. X-ray computed tomography (XCT) [8, 9, 10, 11, 12, 13, 14, 15] is becoming the most adopted technology to verify AM parts. XCT particularly coheres to

AM. In conventional coordinate metrology, an operator has to develop a part program. Performing an XCT scan does not require a part program. At most, setting a series of parameters suffices. This is similar to the automatic or quasi-automatic generation of part programs in AM. Similarly, XCT does not require developing complex and expensive fixtures. As XCT can see inside parts in a non-destructive way, it can study porosity, inclusions, voids, and all internal defects in which AM parts are rich. Finally, XCT is the unique inspection technology that can verify the geometry of complex and internal, or in general inaccessible, surfaces typical of AM parts.

Please note the measurement result of an XCT scan is a voxel representation (XCT image) of the X-ray attenuation inside the volume within which the part falls. To compare the XCT image to a conventional surface representation of the part the common practice is segmenting the image to identify the surface, convert the image to a mesh, and finally compare the mesh to the nominal geometry. Literature widely discusses this methodology with particular focus on the measurement uncertainty evaluation [16, 17, 18, 19, 20, 21, 22, 23, 24, 25]. Therefore, defining conformance and nonconformance rules considering the ISO/IEC guide 98-4 [26] and the ISO 14253-1 standard [27]: using segmentation to verify AM parts geometry is possible. However, segmentation is among the most relevant contributions to the measurement error [28, 29, 30, 31, 32]. Besides, literature describes many techniques for segmentation (ISO50, Otsu's, local thresholding, region growing, Canny's, etc), each one generating a different part surface. A guideline to choosing the correct one is still the subject of research.

However, the output of an XCT scan is a volumetric representation of the part: why not compare the XCT image to the voxel representation of the geometric tolerance, i.e. a representation of maximum and minimum material continuum? The authors of this paper envisage [33] the possibility of a volumetric (and then segmentation-free) geometric inspection, and propose a methodology. However, the difference between this methodology and the conventional segmentation-based approach is significant. Volumetric verification does not yield any measurement results. The only output is a conformance or noncon-

formance statement. This prevents expressing measurement uncertainty and conventional management of the producer's and consumer's risks.

This paper aims to develop an applicable methodology for estimating and managing the producer's and consumer's risks when applying the volumetric geometric inspection. To achieve this aim, the paper follows this structure. §2 describes the proposed methodology in-depth and analyses it theoretically. This allows a complete understanding of its meaning and implications. Although previous works started developing the method, the theoretical dissertation is novel. §3 introduces the error possibilities of the methodology. False rejection and false acceptance are defined in this way. They relate strictly to the definition of the consumer's and producer's risk. Deduction of the theoretical definition of the risks follows. §4 proposes a methodology for an approximate estimate of the risks. It is based on the empirical distribution of the measured X-ray attenuation. Acquiring an XCT image and defining the volumetric tolerance suffices to apply the method. Any a-priori assumption is unnecessary. Evaluating the risks leads to defining a conformance or nonconformance criterion differing from the one proposed in previous papers. Finally, §5 validates the method considering a simple AM case study and comparing the results to the conventional segmentation-based inspection results.

2. Basics of the segmentation free geometric verification

The authors proposed a criterion for the segmentation-free verification of the geometry of parts by X-ray computed tomography in a previous article [33]. To allow the reader to understand the following discussion on the reliability criterion, we report and demonstrate it here in-depth for the sake of completeness.

2.1. Definition of the problem

A voxel representation of a volume is a set of values $v_{i,j,k}$, $i \in \{1, 2, \ldots, n_x\}$, $j \in \{1, 2, \ldots, n_y\}$, $k \in \{1, 2, \ldots, n_z\}$, on a 3D grid. $v_{i,j,k}$ represents some property at a specific coordinate. If the grid spacing along the x direction

is s_x, s_y along y, and s_z along z, the $v_{i,j,k}$ conventional coordinates will be $[i \cdot s_x, j \cdot s_y, k \cdot s_z]$. In most cases voxels are cubic, i.e. $s_x = s_y = s_z = s$. Although the value $v_{i,j,k}$ should punctually refer to coordinates $[i \cdot s_x, j \cdot s_y, k \cdot s_z]$, often it improperly associates with an elementary volume of size s_x, s_y, s_z centered at $[i \cdot s_x, j \cdot s_y, k \cdot s_z]$ of which it represents an average value. The total number of values is $n_{tot} = n_x n_y n_z$.

Let's define the tolerance zone for a volumetric representation of an object. A possible representation is as follows:

- Assign the value a (air) to the portion of the volume that cannot be material-filled (complementary of the maximum material continuum).
- Assign the value m (material) to the portion of the volume that must be material-filled (minimum material continuum).
- Assign the value t (transition) to the portion of the volume that can either be material-filled or not (transition zone).

This allows easy representation of a variable tolerance zone amplitude, as shown in Fig. 1[1]. The latter portion of the volume, equal to t, represents the tolerance zone. Therefore, the voxel representation of the nominal geometry together with its tolerance zone is a 3D array **TV**, each element of which is a value $TV_{i,j,k} \in \{a, m, t\}$. This representation will be called the "volumetric model of the geometric tolerance" (VMGT).

The volumetric representation of the measured object (VRMO) is the result of a volumetric measurement (e.g. by x-ray computed tomography or ultrasonic scan). It is, therefore, a 3D array **GV**. Each value $GV_{i,j,k}$ represents a local property within the volume (in the case of x-ray tomography it is the local x-ray attenuation, which is roughly proportional to the local density). In theory, because, for example, the x-ray attenuation is a continuous quantity, $GV_{i,j,k} \in$

[1] Although this article focuses on the 3D (volumetric) image case, extending the same concepts to the 2D image case is possible.

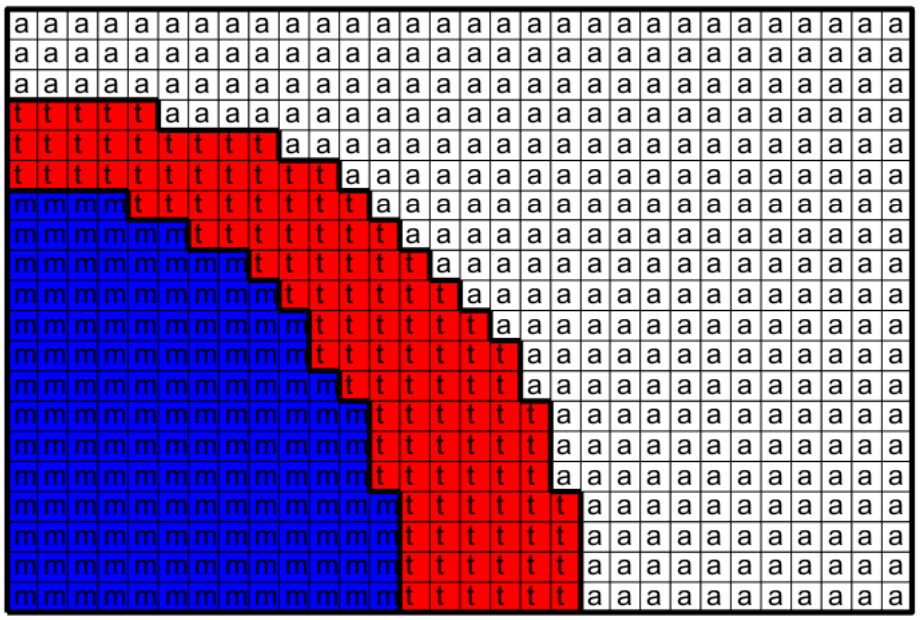

Figure 1: A single slice (image) of a voxel representation of a geometric tolerance zone. Please note the variable amplitude of the tolerance zone.

$\mathbb{R}$. Although the theoretical definition of $GV_{i,j,k}$ is in $\mathbb{R}$, when it is measured an 8, 16, or 32-bit integer variable stores the measurement result. In the following, we will alternatively need to consider it continuous or discrete. Therefore a continuous dissertation describes the theoretical distribution of $GV_{i,j,k}$ (in §3.1), while the measurement result treatise is discrete (§2.2). The maximum value of $GV_{i,j,k}$ in the discrete representation is mv_{max}. The minimum is, of course, equal to 0.

The problem is defining a verification procedure stating whether the VMGT and the VRMO of an object are compatible.

2.2. Proposed approach to the verification of the compatibility of VMGT and VRMO

A previous article [33] justified that volumetric verification is based on the inner and outer shells (Fig. 2). The shells definition follows. Let's introduce the

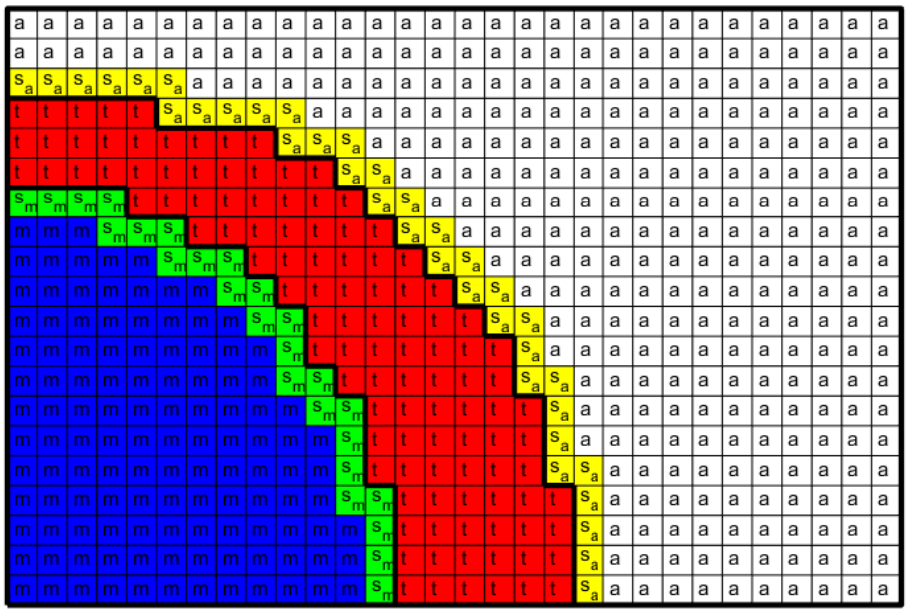

Figure 2: Representation of the inner (green) and outer (yellow) shells.

concept of neighbourhood of a voxel, i.e. the set of voxels next to it:

$$N\left(v_{i,j,k}\right) = \bigcup_{o,p,r \in \{-1,0,1\}} v_{o+i,p+j,q+k} - v_{i,j,k} \tag{1}$$

Here o, p, r are just scalars that alternatively assume the values $\{-1, 0, 1\}$ so that $v_{o+i,p+j,q+k}$ is a voxel adjacent to voxel $v_{i,j,k}$. It is possible to define a "voxel-based model of the geometric tolerance with shells" (VMGTS) as

$$SV_{i,j,k} = \begin{cases} a, & \{\nexists\, TV_{o,p,q} \in N\left\{TV_{i,j,k}\right\} | TV_{o,p,q} = t\} \wedge TV_{i,j,k} = a \\ t, & TV_{o,p,q} = t \\ m, & \{\nexists\, TV_{o,p,q} \in N\left\{TV_{i,j,k}\right\} | TV_{o,p,q} = t\} \wedge TV_{i,j,k} = m \\ s_m, & \{\exists\, TV_{o,p,q} \in N\left\{TV_{i,j,k}\right\} | TV_{o,p,q} = t\} \wedge TV_{i,j,k} = m \\ s_a, & \{\exists\, TV_{o,p,q} \in N\left\{TV_{i,j,k}\right\} | TV_{o,p,q} = t\} \wedge TV_{i,j,k} = a \end{cases} \tag{2}$$

where s_a-valued voxels are part of the outer shell and s_m-valued voxels are part of the inner shell. $TV_{o,p,q} \in N\left\{TV_{i,j,k}\right\}$ should be intended ad a generic voxel in the neighborhood of $TV_{i,j,k}$. For example, line four of (2) is interpreted as "a voxel belongs to the inner shell if its value is equal to m (it belongs to the mini-

mum material continuum) and in its neighborhood there is at least a voxel whose value is t (it belongs to the transition zone)". The outer shell demonstrates that it is a subset of the complementary of the maximum material continuum, and the inner shell a subset of the minimum material continuum. Set NSN_I defines points belonging to the inner shell in the VMGT, and, similarly, set NSN_O defines points belonging to the outer shell. Define $NSN = NSN_I \cup NSN_O$. Suppose that the VMGT and VRMO share the same voxel size and volume. In this case each voxel of the VMGT (and then of the VMGTS) corresponds to a voxel of the VRMO. It is then possible to define the sets of VRMO voxels corresponding to the VMGTS inner and outer shells as NSM_I and NSM_O respectively, and $NSM = NSM_I \cup NSM_O$. Finally, let's define n_i as the number of values in NSN_I, n_o as the number of values in NSN_O, and $n_i + n_o = n$.

The verification of the volumetric tolerance of the part is a comparison between NSN and NSM. The comparison will be based on the information contained in the two sets. In general, the information in NSN is smaller than the information in NSM. The first is noise-free, so its value is constant within the inner/outer shell. The differential entropy H [34] measures the information for a set of values, when considered as a signal taking a random value Q, and described by the continuous probability density $f(q)$ [34]:

$$H = -\int_{-\infty}^{+\infty} f(q) \log_2 f(q) dq \tag{3}$$

According to (2), in NSN q assumes only two possible values s_a and s_m. This justifies choosing the value 2 as an exponent of the logarithm in (3).

Calculating the differential entropy in (3) would be possible if the real statistical distribution of values inside the voxels was available. This is true in the case of NSN, which has a nominal definition (although this random variable discrete nature makes reference to Shannon's entropy, introduced later in this section, preferable). The real distribution of the measured values of $GV_{i,j,k}$ in NSM cannot be available.

Consider NSN and NSM as sorted lists of values. As defined in §2.1, NSN and NSM assume only integer positive values. In the case of NSM, define

n_m as the number of occurrences of value m in NSM. Shannon's entropy [35] measures the information content of NSM. An estimate of it is appraisable from the XCT image as:

$$\hat{H}(NSM) = -\sum_{m=0}^{mv_{max}} \frac{n_m}{n} \log_2 \frac{n_m}{n} \tag{4}$$

The case of NSN is simpler, as NSN is nominally defined and assumes only the values s_a (n_o times) and s_m (n_i times). Furthermore, this is a theoretical value: NSN is nominally defined. Therefore, the actual value of $H(NSN)$ is:

$$H(NSN) = -\frac{n_i}{n} \log_2 \frac{n_i}{n} - \frac{n_o}{n} \log_2 \frac{n_o}{n} \tag{5}$$

Please note that, as typically $n_i \simeq n_o \simeq \frac{n}{2}$, usually it will be $H(NSN) \simeq 1$, which further justifies choosing the value 2 as a logarithm base for the entropy.

These equations indicate that, except degenerate cases, $\hat{H}(NSM) > H(NSN)$. This is due to NSM being a representation a part of the real object, so it contains also information on e.g. the local density. NSN instead contains only information on the geometry of the part. However, this does not imply necessarily that NSM contains all the information in NSN.

Now, the only information conveyed by NSN is that "complete separation occurs between the shells", as they do not share any value (the inner shell contains the value s_m and the outer shell contains the value s_a, no shared values). As such, if the NSM contains all the information in NSN, the VRMO contains the full separation information as well: this condition verifies conformance to the geometric tolerance. In fact, this would mean that the NSM_I and the NSM_O are somehow separated, completely different from the point of view of the $GV_{i,j,k}$ they contain.

To verify if NSM contains all the information in NSN mutual information is the key. Mutual information (Fig. 3) measures the information shared by two signals. First, to explain it, let's introduce Shannon's entropy of a joint distribution to explain it. Suppose $f(mv, nv)$ is the joint distribution of the measured values MV in NSM and nominal values NV in NSN. Considering

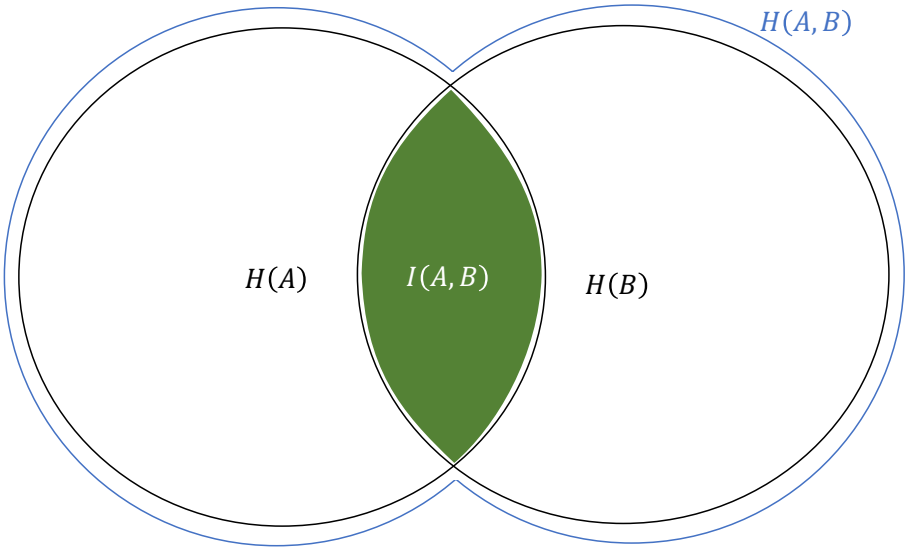

Figure 3: Relationship between entropy, joint entropy, and mutual information.

that nv assumes two possible values s_a, s_m define the joint differential entropy of NSM and NSN as:

$$\begin{aligned} & H\left(NSM, NSN\right) = \\ & = - \sum_{nv \in \{s_a, s_m\}} \int_{-\infty}^{+\infty} f\left(mv, nv\right) \log_2 \left[f\left(mv, nv\right)\right] dmv \end{aligned} \tag{6}$$

The joint entropy measures the total information contained in two signals, both shared and unshared.

Again, no ambiguity in the values NV in NSN, but MV in NSM is distributed according to an unknown statistic. An estimate of the joint Shannon's entropy of NSN and NSM originates from the XCT image as:

$$\begin{aligned} \hat{H}\left(NSN, NSM\right) = & - \sum_{m=0}^{mv_{max}} \frac{n_{s_a,m}}{n} \log_2 \frac{n_{s_a,m}}{n} - \\ & - \sum_{m=0}^{mv_{max}} \frac{n_{s_m,m}}{n} \log_2 \frac{n_{s_m,m}}{n} \end{aligned} \tag{7}$$

where $n_{q,m}$ is the number of times a voxel in NSN assumes the value q, $q \in \{s_a, s_m\}$, and the corresponding voxel in NSM assumes the value m.

Define the mutual information as:

$$I(A,B) = H(A) + H(B) - H(A,B) \tag{8}$$

The condition for which NSM contains all the information of NSN is:

$$I(NSN, NSM) = H(NSN) \tag{9}$$

or, equivalently:

$$H(NSN, NSM) = H(NSM) \tag{10}$$

To verify whether the XCT measurement result satisfies this condition, substitute (4) and (7) into (10):

$$-\sum \frac{n_m}{n} \log_2 \frac{n_m}{n} = -\sum \frac{n_{s_m,m}}{n} \log_2 \frac{n_{s_m,m}}{n} - \sum \frac{n_{s_a,m}}{n} \log_2 \frac{n_{s_a,m}}{n} \tag{11}$$

Considering that, due to the properties of the logarithms, $\log_2 \frac{n_m}{n} = \log_2 n_m - \log_2 n$, and that $\sum n_m = n$, the first member of (11) turns into:

$$-\sum \frac{n_m}{n} \log_2 \frac{n_m}{n} = -\sum \frac{n_m}{n} \log_2 n_m + \log_2 n \tag{12}$$

Applying a similar elaboration to the other terms of (11), and remembering that $n_m = n_{s_a,m} + n_{s_m,m}$, which also implies that:

$$\sum (n_{s_m,m} + n_{s_a,m}) = n \tag{13}$$

(11) simplifies into:

$$\sum n_m \log_2 n_m = \sum n_{s_m,m} \log_2 n_{s_m,m} + \sum n_{s_a,m} \log_2 n_{s_a,m} \tag{14}$$

which expands into:

$$\begin{aligned} \sum n_m \log_2 n_m &= \sum n_{s_m,m} \log_2 \frac{n_m n_{s_m,m}}{n_m} + \sum n_{s_a,m} \log_2 \frac{n_m n_{s_a,m}}{n_m} = \\ &= \sum n_{s_m,m} \log_2 \frac{n_{s_m,m}}{n_m} + \sum n_{s_a,m} \log_2 \frac{n_{s_a,m}}{n_m} + \\ &\quad + \sum (n_{s_m,m} + n_{s_a,m}) \log_2 n_m \end{aligned} \tag{15}$$

As $n_{s_a,m} + n_{s_m,m} = n_m$, (15) finally leads to:

$$\sum n_{s_m,m} \log_2 \frac{n_{s_m,m}}{n_m} + \sum n_{s_a,m} \log_2 \frac{n_{s_a,m}}{n_m} = 0 \tag{16}$$

All terms in summations of (16) are negative or null at most. Therefore, (16) or equivalently (9) holds when all the terms are equal to zero. A term of these is null if one of the following conditions holds: $n_{s_m,m} = 0$, $n_{s_a,m} = 0$, $n_{s_m,m} = n_m$, or $n_{s_a,m} = n_m$. Remembering again that $n_{s_a,m} + n_{s_m,m} = n_m$, it follows that this happens if both the following two conditions hold:

$$\begin{aligned} n_{s_a,m} \neq 0 \Rightarrow \quad & n_{s_a,m} = n_m, \quad n_{s_m,m} = 0 \\ n_{s_m,m} \neq 0 \Rightarrow \quad & n_{s_m,m} = n_m, \quad n_{s_a,m} = 0 \end{aligned} \tag{17}$$

The inverse demonstration from (17) to (9) follows by substituting (17) into (4), (5), and (7).

The equivalence between conditions (17) and condition (9) translates into: NSM contains all the information in NSN if and only if NSM_O and NSM_I have no common value. A specific case of conditions (17) clarifies the concept:

$$\forall GV_{i,j,k} \in NSM_I \nexists\, gv_{o,p,q} \in NSM_O | gv_{o,p,q} \geq GV_{i,j,k} \tag{18}$$

i.e. NSM_I contains all large values and NSM_O contains all small values[2].

that is, all large values are found in NSM_I and all small values are found in NSM_O[3].

3. Reliability of the segmentation-free verification

After defining a criterion to distinguish conforming parts from nonconforming parts, the next step is calculating the probability of the criterion failing in

[2]If low values of $GV_{i,j,k}$ characterize material-filled voxels and high values of $GV_{i,j,k}$ characterize air-filled voxels the condition changes slightly: (18) would just change into $\forall GV_{i,j,k} \in NSM_I \nexists\, gv_{o,p,q} \in NSM_O | gv_{o,p,q} \leq GV_{i,j,k}$.

[3]If material-filled voxels are characterized by low value of $GV_{i,j,k}$ and air-filled voxels are characterized by high values of $GV_{i,j,k}$ the concept would be similar anyway, i.e. (18) would just change into $\forall GV_{i,j,k} \in NSM_I \nexists\, gv_{o,p,q} \in NSM_O | gv_{o,p,q} \leq GV_{i,j,k}$.

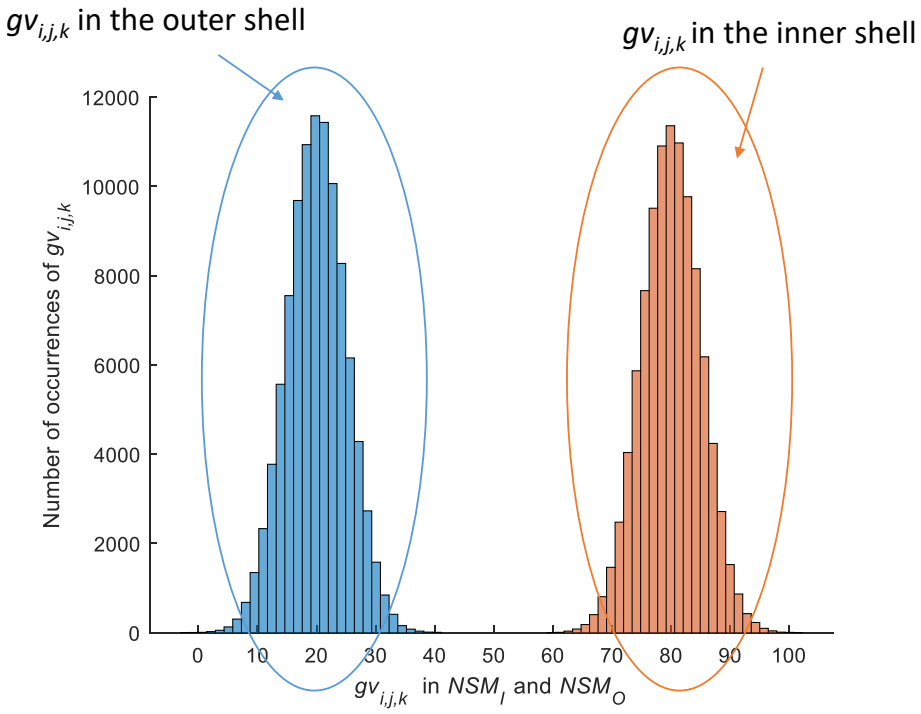

Figure 4: Complete separation of the inner and outer shells.

identifying part conformance. Let's start by introducing the situations where the criterion succeeds in categorizing parts.

First, the histogram in Fig. 4 exemplifies a case where the criterion states that a conforming part conforms: the two histograms of the values in the inner/outer shells show no shared value. This is what one expects when the part satisfies the tolerance: the shells are clearly distinct from one another. Let's move to nonconforming conditions. Consider Fig. 5: in this case, the distributions of the $GV_{i,j,k}$ in the inner and outer shells overlap: the criterion in (9) declares the part to be nonconforming. This is the case when the part presents a size deviation. For example, suppose adding excessive material to the product: the material fills the maximum material continuum and overflows into the surrounding volume. As the voxels immediately off the maximum material continuum constitute the outer shell, this is the first volume portion the exceeding

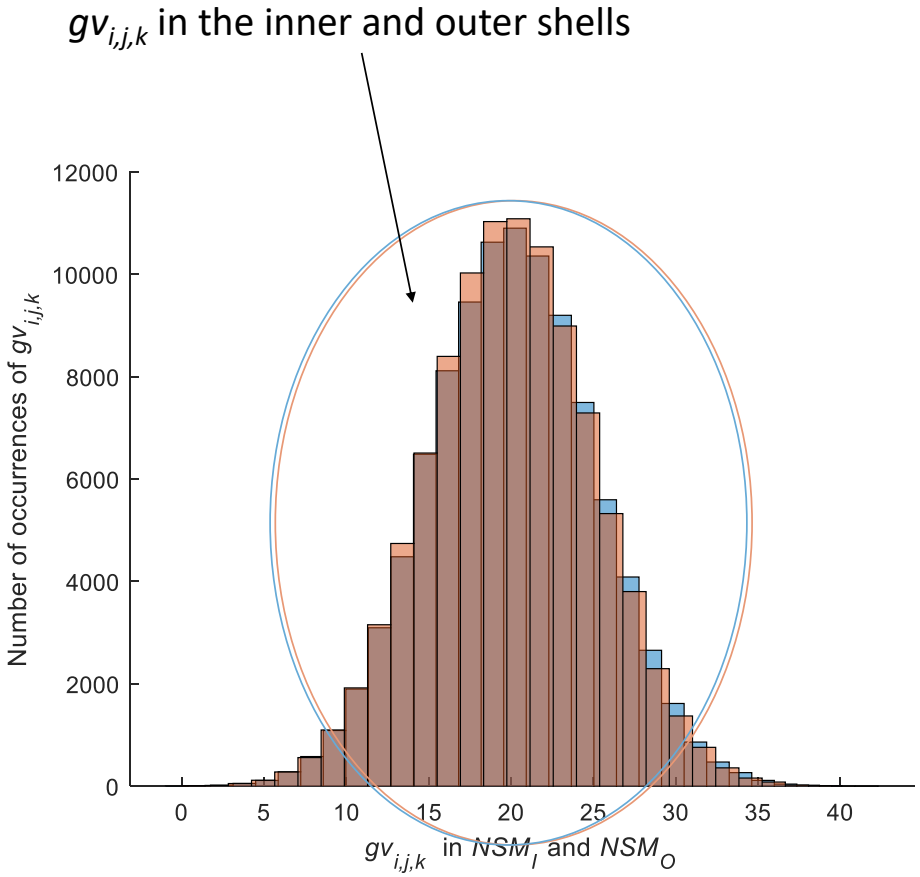

Figure 5: Size deviation in the part: the distributions of $GV_{i,j,k}$ in the inner and the outer shells overlap.

material fills. Therefore, the outer shell presents a distribution of the $GV_{i,j,k}$ similar to the material-filled inner shell. A similar reasoning applies when the added material is insufficient. Finally, consider Fig. 6: although the distributions of $GV_{i,j,k}$ in the two shells are different, they overlap, and the criterion in (9) declares again that the part does not conform. These typical histograms indicate a part presenting a geometric deviation. Although the material quantity is adequate (sufficient to fill the minimum material continuum but insufficient to exceed the maximum material continuum), the part shape deviates from nominal. Therefore, the shells contain both material and air. Of course, a part

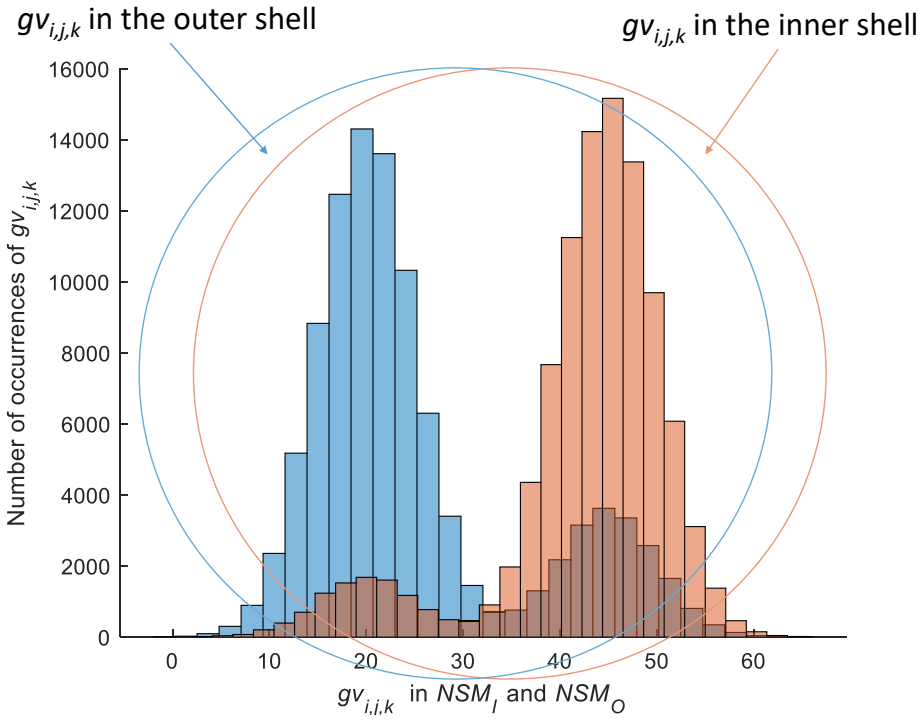

Figure 6: Geometric deviation in the part: the distributions of $GV_{i,j,k}$ in the inner and the outer shells are different, yet partially overlapped.

characterized by this shell situation is defective.

In all these conditions the criterion in (9) should identify the conformance or nonconformance of the part. But of course, as with any decision criterion, the criterion can fail in categorizing the part. Consider for example the case in Fig. 7: no shared value in the histograms. As NSM_I and NSM_O do not share any value, they satisfy condition (9). But complete shell overlap is evident and values shown in NSM_I and NSM_O are close. In this case, one can say that the proposed verification method fails and a nonconforming part is stated to be conforming. Then, consider Fig. 8: in this case a single $GV_{i,j,k}$ from the inner shell overlaps with the outer shell. One could argue that the part conforms to the geometric tolerance, and the overlapping $GV_{i,j,k}$ is an outlier, but there is no way of demonstrating it, and mathematically it does not meet condition (9): a con-

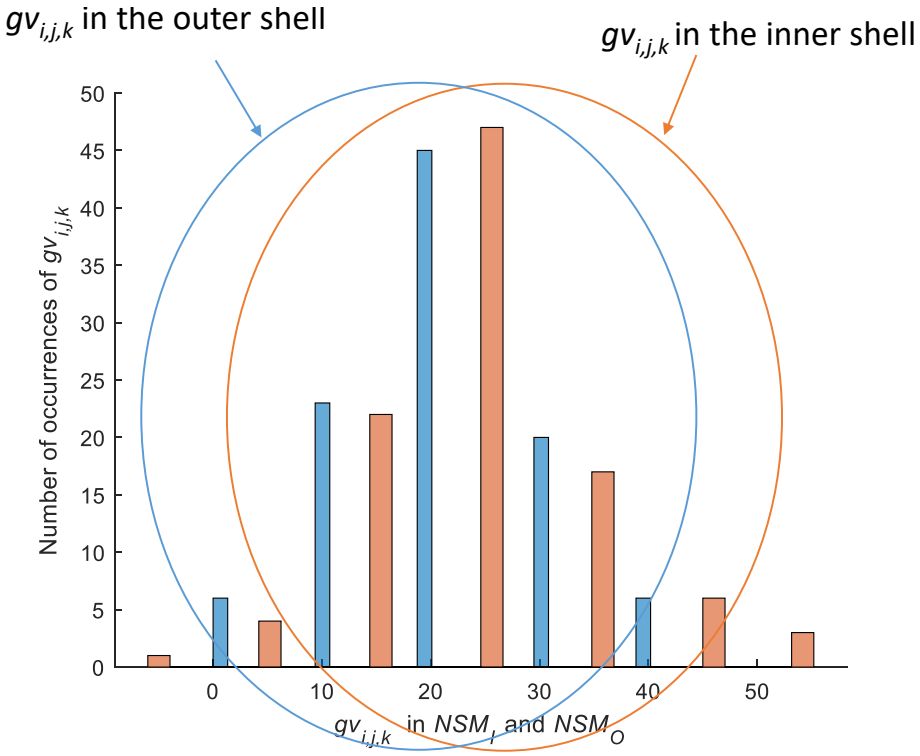

Figure 7: A false acceptance case: no clear distinction between the shells, but no shared values, so the distributions satisfy condition (9).

forming part is stated to be nonconforming. These two examples demonstrate that the decision rule proposed by the authors in a previous paper [33] can fail in identifying the conformance or nonconformance of parts. This is common to all possible decision rules. Tab. 1 summarizes the possible test results [26]: two types of errors are possible, i.e. false rejection (declaring a conforming part to be nonconforming) and false acceptance (declaring a nonconforming part to be conforming). ISO/IEC Guide 98-3 Part 4 [26] assigns false rejections to the consumer's risk (probability of accepting a nonconforming item based on a future measurement result), and false acceptances to the producer's risk (probability of rejecting a conforming item based on a future measurement result). In this sense, Fig. 7 is an example of false acceptance, and Fig. 8 is an example of false rejection.

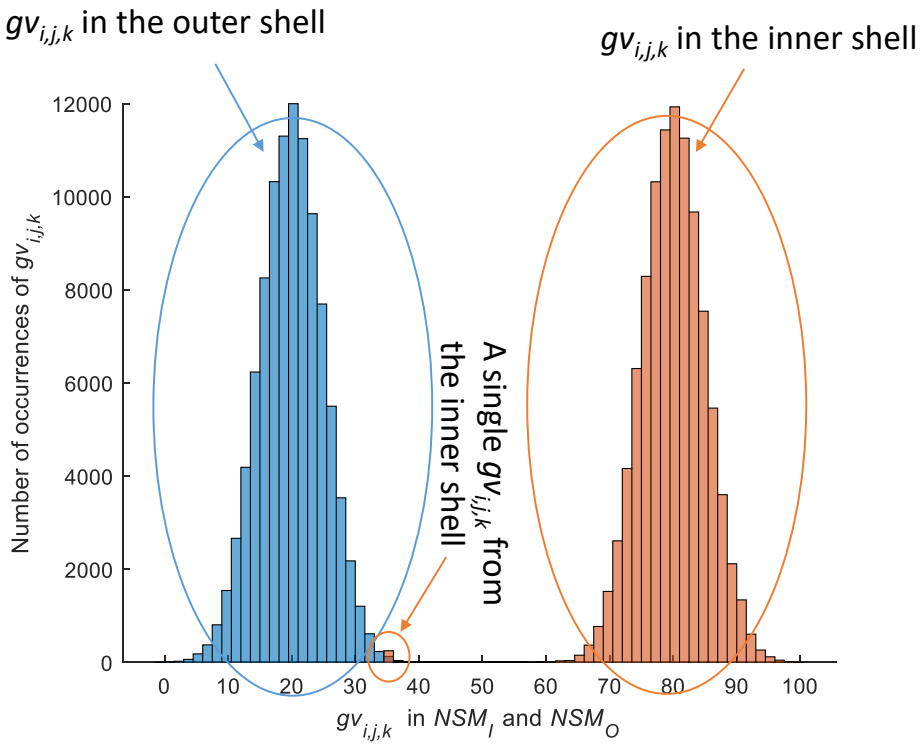

Figure 8: A false rejection case: the shells show different distributions, but do not meet condition (9).

ISO/IEC Guide 98-3 Part 4 requires that a complete decision rule defines "how measurement uncertainty will be accounted for with regard to accepting or rejecting an item". Uncertainty represents a measurement result typical dispersion. Dispersion generates the risks (a dispersion-free measurement would generate a risk-free decision rule). Therefore, the guide asks that the consumer's and/or and producer's risks be taken into account in the decision rule. Conventional decision rules are based on measurement results and their comparison to specification limits, considering the uncertainty, and defining a guard band. In the case of the proposed criterion, this is impossible. Condition (9) avoids any measurement result, so no uncertainty statement is possible. Neither is any conventional guard band approach.

However, this does not exclude considering consumer's and producer's risks,

	Condition (9) is met	Condition (9) is not met
The part conforms to the specified geometric tolerance	*Valid acceptance*	**False rejection**
The part does not conform to the specified geometric tolerance	**False acceptance**	*Valid rejection*

Table 1: Conformance verification: possible errors.

thus proposing a rule that conforms to ISO/IEC Guide 98-3 part 4. Let's derive their mathematical definition when applying segmentation free verification. This requires a mathematical definition of what a conforming or nonconforming part is, considering criterion (9). It will slightly differ from the definition in (17).

3.1. Mathematical definition of a conforming part

§2 defined how to estimate $H(NSM)$ and $H(NSM, NSN)$. The event "the part is conforming" corresponds to the condition in which the real values of $H(NSM)$ and $H(NSM, NSN)$ exist, are known, and satisfy (10).

The definition of $H(NSM, NSN)$ is in (6). For $H(NSM)$, let's assume some hypotheses. Define $f_I(GV)$ as the statistical distribution of the GV in the inner shell and $f_O(GV)$ as the statistical distribution of the GV in the outer shell (no specific assumption on the type of distribution is needed). The two distributions can be identical (Fig. 5 and 7) or different (Fig. 4, 6, and 8). Let's assume also that in the inner shell GV can assume all possible values in the domain $[L_I, U_I]$, and in the outer shell GV can assume all possible values in the domain $[L_O, U_O]$. This means GV assumes values within limited intervals

$[\min\{L_I, L_O\}, \max\{U_I, U_O\}] = [L, U]$. From the point of view of the statistical density, this implies that:

$$\begin{aligned} GV \notin [L_I, U_I] \Rightarrow \quad & f_I(GV) = 0, \quad GV \in (L_I, U_I) \Rightarrow \quad f_I(GV) > 0 \\ GV \notin [L_O, U_O] \Rightarrow \quad & f_O(GV) = 0, \quad GV \in (L_O, U_O) \Rightarrow \quad f_O(GV) > 0 \end{aligned} \tag{19}$$

Remembering the NSN structure, and applying the law of total probability, the distribution of the shells considered together is then

$$f(GV) = \frac{n_I}{n} f_I(GV) + \frac{n_O}{n} f_O(GV) \tag{20}$$

Let's study under which circumstances the following equality, originating from substituting (6) and (20) into (10), holds:

$$\begin{aligned} & -\sum_{nv \in \{s_a, s_m\}} \int_I^U f(GV, nv) \log_2 [f(GV, nv)] dGV = \\ & = -\int_L^U \left[\frac{n_I}{n} f_I(GV) + \frac{n_O}{n} f_O(GV)\right] \log_2 \left(\frac{n_I}{n} f_I(GV) + \frac{n_O}{n} f_O(GV)\right) dGV \end{aligned} \tag{21}$$

Consider $f(GV, nv)$. From their definition it follows that $f_I = f_{MV|NV=s_m}(GV)$ and $f_O = f_{MV|NV=s_a}(GV)$, i.e $f_I(GV)$ and $f_O(GV)$ are the conditional distributions of GV given NV. Taking into account the definition of conditional distribution, $f(GV, nv)$ can changes into:

$$f(GV, nv) = \begin{cases} \frac{n_I}{n} f_I(GV), & nv = s_m \\ \frac{n_O}{n} f_O(GV), & nv = s_a \end{cases} \tag{22}$$

Substituting this definition into (21) the following new expression of condition

(10) derives:

$$\begin{aligned}
&\int_{L_I}^{U_I} \frac{n_I}{n} f_I(GV) \log_2 \frac{n_I}{n} f_I(GV) \, dGV + \\
&+ \int_{L_O}^{U_O} \frac{n_O}{n} f_O(GV) \log_2 \frac{n_O}{n} f_O(GV) \, dGV = \\
&= \int_{L}^{U} \frac{n_I}{n} f_I(GV) \log_2 \left[\frac{n_I}{n} f_I(GV) + \frac{n_O}{n} f_O(GV) \right] dGV + \\
&+ \int_{L}^{U} \frac{n_O}{n} f_O(GV) \log_2 \left[\frac{n_I}{n} f_I(GV) + \frac{n_O}{n} f_O(GV) \right] dGV = \\
&= \int_{L_I}^{U_I} \frac{n_I}{n} f_I(GV) \log_2 \left[\frac{n_I}{n} f_I(GV) + \frac{n_O}{n} f_O(GV) \right] dGV + \\
&+ \int_{L_O}^{U_O} \frac{n_O}{n} f_O(GV) \log_2 \left[\frac{n_I}{n} f_I(GV) + \frac{n_O}{n} f_O(GV) \right] dGV
\end{aligned} \tag{23}$$

Remembering that density functions are positive or at most null, and the logarithm is a monotonic increasing function, it is easy to demonstrate that the equality in (23) holds only if these conditions hold:

$$\begin{aligned}
GV \in [L_I, U_I,] \Rightarrow \quad & f_O(GV) = 0 \\
GV \in [L_O, U_O,] \Rightarrow \quad & f_I(GV) = 0
\end{aligned} \tag{24}$$

Demonstrating that, if condition (24) holds, condition (10) holds immediately followes by substituting (24) into (23).

The previous demonstration shows that, under the assumption in (20), the "full separation" information contained in NSN belongs also to NSM if and only if the definition intervals of the statistical distributions of the shells $[L_I, U_I]$ and $[L_O, U_O]$ do not share any value, or equivalently

$$L_O > U_I \vee L_I > U_O \tag{25}$$

This demonstration has lead to a result similar to the one expressed in (17) and (18). Again, the condition is "no shared value". This real conformance case, however, considers that the X-ray attenuation measured by XCT assumes values in $\mathbb{R}$, and the separation must concern the definition domains. In practice conformance definition of a part is summarized in:

> The part conforms to a VMGT if the definition domains of the the statistical distributions of the X-ray attenuation within the inner and outer shell respectively do not share any value.

This is coherent with the inner shell being material-filled and the outer shell air-filled. Air and material should generate non-overlapping statistical distributions of X-ray attenuation. It is worth noting that an increase of the measurement noise increases the dispersion of the GV. This in turn enlarges the intervals $[L_I, U_I]$ and $[L_O, U_O]$, making a part conformance statement less likely. This is coherent with the effect of noise in conventional coordinate metrology when verifying a geometric tolerance: the noise increases the measured global deviation, and the part is less likely to be stated conforming.

3.2. Consumer's and producer's risks. Conformance probability

Having defined what conformance to a volumetric geometric tolerance means, it is possible to mathematically express the consumer's and producer's specific risks.

The specific consumer's risk is expressed as:

$$R_{\mathrm{C}}^{*} = P\left(\hat{I}\left(NSM, NSN\right) = \hat{H}\left(NSN\right) | L_O \leq U_I \vee L_I \leq U_O\right) \tag{26}$$

and the specific producer's risk:

$$R_{\mathrm{P}}^{*} = P\left(\hat{I}\left(NSM, NSN\right) \neq \hat{H}\left(NSN\right) | L_O > U_I \vee L_I > U_O\right) \tag{27}$$

The ISO 14253-1 standard [27] proposes the following as a default rule for proving conformance:

> As measured values include uncertainty, any decision based on them is subject to a risk of being false. The conformance probability is the probability that the true value falls inside the specification zone. Setting a decision rule such that an item is accepted if the conformance probability is above a conformance probability limit (e.g. 95%) effectively confines the risk of false decision to the complement of such conformance probability limit (e.g. 5%).

According to the ISO/IEC Guide 98-3 Part 4, the mathematical definition of the conformance probability is:

$$p_c = P\left(Y \in C | \eta_m\right) \tag{28}$$

where Y is the real value of a measurable property of the product, C is the set of admissible values for Y, and η_m is the measured quantity value. Please note this definition is identical to the definition of R_{C}^* when the part is nonconforming, or $1 - R_{\mathrm{P}}^*$ when the part is conforming.

Modifying (28) by removing the need for a measured value, this approach is applied to the proposed decision rule. The default rule shall be redefined as follows:

> As *mutual information estimates are approximations of its real value*, any decision based on them is subject to a risk of being false. The conformance probability is the probability that *the definition intervals of the statistical distributions of the shells* $[L_I, U_I]$ *and* $[L_O, U_O]$ *do not share any value, given the actual XCT image and in particular* NSM *and* NSN. Setting a decision rule such that an item is accepted if the conformance probability is above a conformance probability limit $1-\alpha$ (e.g. 95%) effectively confines the risk of false decision to the complement of such conformance probability limit (e.g. 5%).

which mathematically translates into:

$$p_c = P\left(L_O > U_I \vee L_I > U_O | NSM\right) \geq 1 - \alpha \tag{29}$$

A similar nonconformance decision rule is definable.

This new form of the decision rule allows some considerations on the actual meaning of distributions in Fig. 7 and 8. Consider for instance Fig. 7. As explained, if condition (9) applies this distribution of $GV_{i,j,k}$ leads to a conformity statement. However, p_c should be low in this case, thus indicating, according to the decision rule, a nonconformity. Similarly, in the case of Fig. 8, the judgment

should be a nonconformance caused by a single outlier value. In this case p_c should be high, leading to a conformance statement. All situations in Fig. 4, 5, and 6 should not pose any problem, as the conformity probability should be either high (Fig. 4) or low (Fig. 5 and 6). This coheres with the result from direct application of condition (9).

4. Estimate of conformance probability: simulation

Calculating p_c is theoretically possible knowing the conditional distributions of $L_O - U_I$ and $L_I - U_O$ given the actual NSM. Arguably, this knowledge is impossible to gather in practice. Let's propose a different approach.

First, please consider that, in general, NSM contains many values - even for small XCT images thousands or millions of voxels constitute the shells. With this large amount of data, empirically estimating the statistical distribution of $GV_{i,j,k}$ in both NSM_I and NSM_O ($f_{e,NSM}(GV_{i,j,k})$) is possible with a good degree of accuracy. This knowledge is still insufficient to estimate p_c; however, it allows the evaluation of

$$p'_c = P\left(\hat{I}(NSM, NSN) = \hat{H}(NSN) \,|f_{e,NSM}(GV_{i,j,k})\right) \tag{30}$$

that is, the probability of stating a part to be conforming, regardless of its conformance. Although this differs from the p_c commonly used in defining binary decision rules, the reader can see that it relates to the specific consumer's and producer's risk. Therefore, a decision rule based on p'_c fulfills the need of considering the risk, the real basis of ISO/IEC Guide 98-3 Part 4. Besides, the uncertainty-based guard-bands conventional approach needs an estimate of the uncertainty. An uncertainty estimate requires assumptions on the statistical distribution of the measurement error. In this sense, although the proposed method is in part incoherent with the definition of the producer's and consumer's risk, it can still be accurate as the conventional approach.

The proposed decision rule follows.

- To prove nonconformance, it is imperative to control the risk of stating a conforming part to be nonconforming, R^*_{P}. Then, a part is stated nonconforming if $p'_c \leq \alpha$, where α is an agreed level for R^*_{P}, otherwise, it is stated to be conforming.

- To prove conformance, it is imperative to control the risk of stating a nonconforming part to be conforming, R^*_{C}. Then, a part is stated conforming if $p'_c \geq 1 - \beta$, where β is an agreed level for R^*_{C}, otherwise, it is stated to be nonconforming.

It is worth noting that as the proposed approach does not yield a measurement result, it is not directly comparable to the conventional approach for the verification of geometric tolerances. Actually, please consider that the proposed methodology bases on a volumetric representation of tolerance, rather than a conventional surface representation of them.

Let's introduce a methodology to empirically estimate the statistical distribution of $GV_{i,j,k}$ and evaluate p'_c. Fig. 9 proposes the steps to apply the methodology in a flux diagram. Please note that, in general, the VRMO and the VMGT must be registered before the method can be applied. The registration error is considered part of the measurement error.

4.1. Estimation of empirical distribution

To perform a simulation of the measured values, let's estimate the probability density function of the values in two shells. Given a set of discrete points, a possible method to estimate the continuous probability density function is the kernel density estimation (KDE) method [36]. Let $\{mv_i\}_{i=1}^n$ be the measured data of the outer or the inner shell, the density can be estimated using the kernel smoothing as:

$$\widehat{f}_{\bullet,KDE}(mv) = \frac{1}{n}\sum_{i=1}^{n} K_h(mv - mv_i), \quad K_h(t) = \exp\left\{-\frac{t^2}{2\,h}\right\} \tag{31}$$

where $K_h(t)$ is the Gaussian kernel function and $\bullet$ can be I or O for either the inner and outer shell. Each value of the density is computed as a weighted

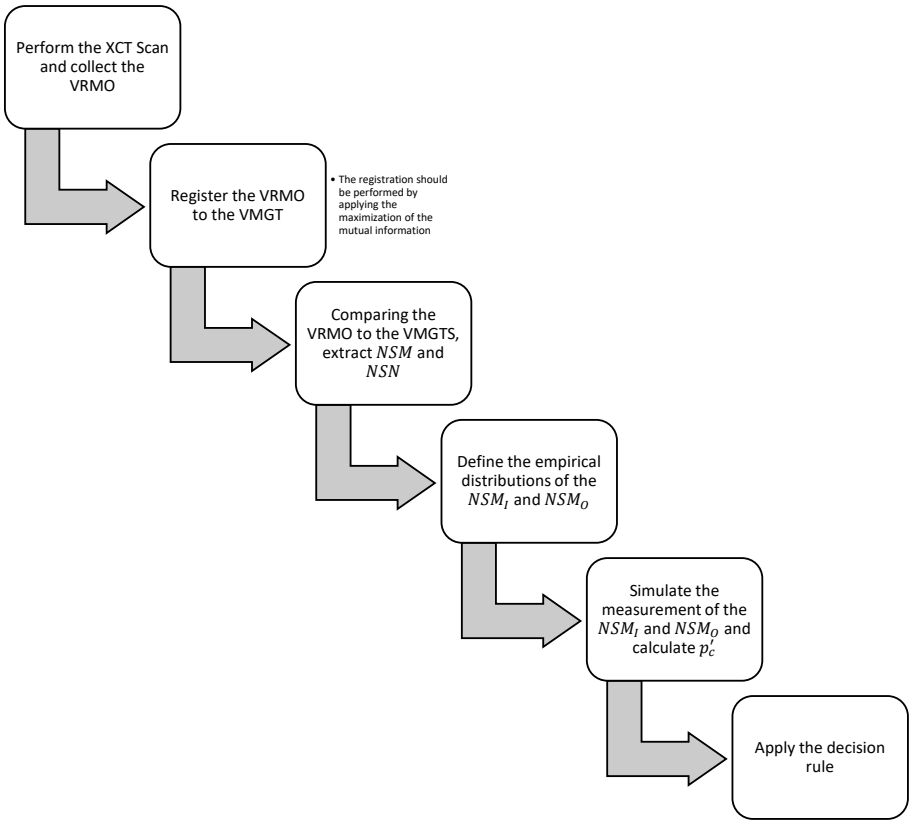

Figure 9: Flux diagram of the proposed methodology.

average of the points in its neighborhood. It is worth noting that the formula in (31) refers to the estimated value, the noise is filtered during the local smoothing process. Parameter h, called bandwidth, is to be set. It controls the neighborhood width of each point t: a higher value for h will result in a larger number of points used in the smoothing process. All points within a distance of about $\pm 3\,h$ from the point t influence the estimate of the density value at t. Each point has a weight equal to $K_h(t)$ on the estimation of the density in mv (the closer the point to mv the larger the influence on the estimate). The weight decreases as the distance from mv increases. Although various automatic methods to estimate the bandwidth are in literature, they are usually optimal for a uni-modal distribution [37]. Considering the possible high variability of the

density functions to be analyzed, and the high amount of data available, let's adopt a fixed value for the bandwidth equal to 0.5 % of the value range. The selected value makes it possible to both perform a smooth estimation of the unknown density function and to follow the local extremes of the curve. Small variations of the tested percentage, such as 1 %, generate a negligible difference in the estimated densities. Conversely, if this value is too high (small) it would lead to a smooth (rough) density: the curve will remove some details of the function or it would follow the data too much.

The estimated KDE can evaluate the values in the central portion of the density function and approximate the various peaks and valley. This method, due to its local nature, may be insufficient to perform a good approximation of the tails of the distribution. To make a value lower than the smallest measured value possible, let's use the generalized Pareto distribution to estimate the tails of the density function. Three parts constitute the density function: a parametric technique estimates the tails, and KDE deals with the central part:

$$\widehat{f}_{\bullet}(mv) = \begin{cases} \widehat{f}^{l}_{\bullet,Pareto}(mv) & \text{if } mv < q_l \\ \widehat{f}_{\bullet,KDE}(mv) & \text{if } q_l \leq mv \leq q_u \\ \widehat{f}^{u}_{\bullet,Pareto}(mv) & \text{if } mv > q_u \end{cases} \tag{32}$$

where $\widehat{f}^{l}_{\bullet,Pareto}(mv)$ and $\widehat{f}^{u}_{\bullet,Pareto}(mv)$ are the lower and upper Pareto distributions used to estimate the tails of the distribution, q_l and q_u are two quantiles discriminating the segments of the distribution. To estimate each tail, the `paretotails` function implemented in Matlab™ [38] suggests using the maximum likelihood estimation [39]. Fig. 10 shows an example of density function estimation. The selected quantiles for q_l and q_u were 10 % and 90 %. Given the independent estimation of the three segments, although the cumulative function is continuous, its density function can be discontinuous. The joining point in Fig. 10b shows a discontinuity. This discontinuity leads to a wrong estimation of the measured values in the shells. To overcome the possible discontinuity of

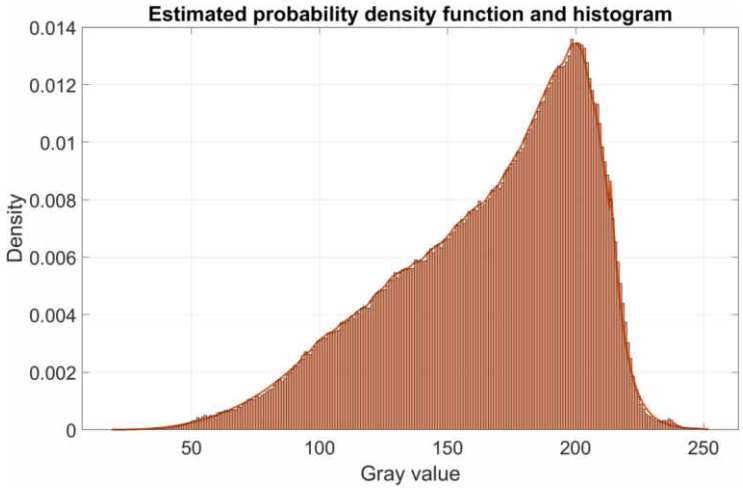

(a) Histogram and estimated KDE

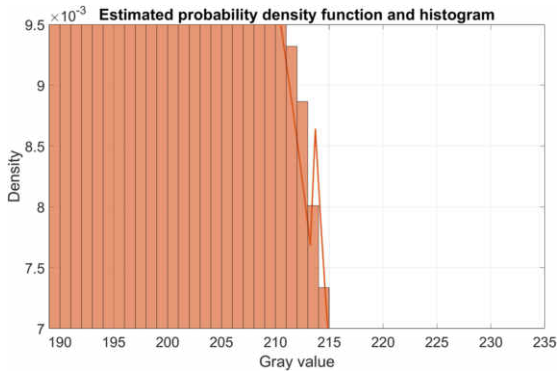

(b) Magnification in the joining point

Figure 10: Histogram and estimated KDE and magnification of the joining point

the density function, the log-likelihood can be modified as:

$$l_{\bullet}^{\star} = l_{\bullet} \cdot \left(1 - \frac{\left| \widehat{f}_{\bullet,KDE}(q_i) - \widehat{f}^{i}_{\bullet,Pareto}(q_i) \right|}{\max\left\{ \widehat{f}_{\bullet,KDE}(q_i), \widehat{f}^{i}_{\bullet,Pareto}(q_i) \right\}} \right) \tag{33}$$

where i refers to either the lower (l) or upper (u) tail. To force the optimization to penalize discontinuities, trying to force a continuous density, let's add a penalty. Fig. 11 shows the estimation of the density function. It is impossible to note the step between the two segments (see Fig. 11b). Note that, due to the

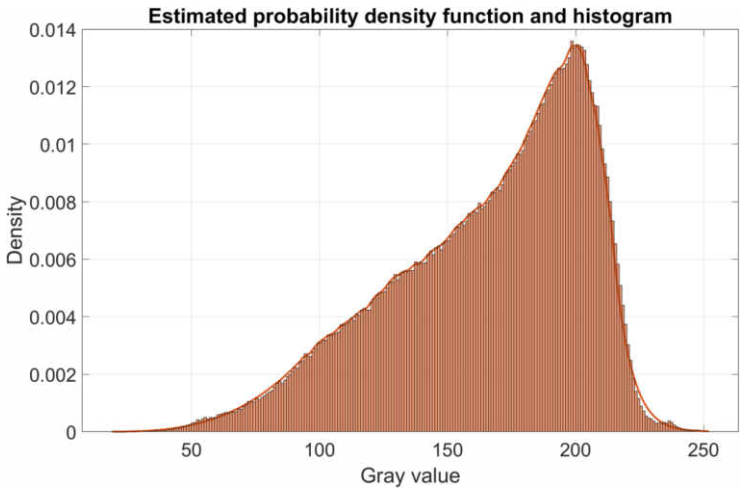

(a) Histogram and estimated KDE

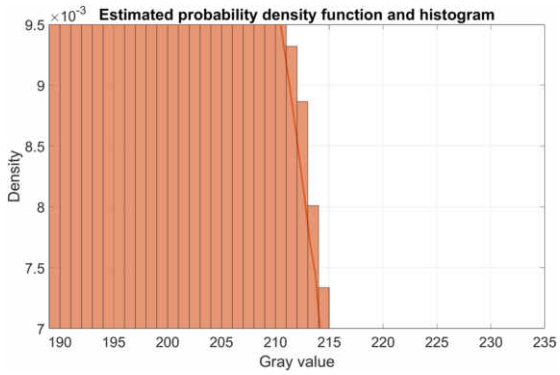

(b) Magnification in the joining point

Figure 11: Histogram and estimated KDE and magnification of the joining point after applying the correction

peak, estimation of the tails is poor. Setting a lower (higher) value of q_l (q_u) avoids this.

It is worth noting that the two types of tests (conformance or nonconformance of the part) require different assumptions on the distributions.

- When proving nonconformance, the base assumption is that the part is conforming, and one looks for proof of nonconformance. As the part conformance statement is likely with limited statistical distributions in the

inner and outer shells, assume limited distributions when estimating them. It is worth noting that, if the supports of two resulting distributions are separated, we have $p'_c = 1$. This coheres with the proposed criterion for stating nonconformance $p'_c \leq \alpha$, discouraging nonconformance statements.

- When proving conformance, the base assumption is that the part is nonconforming, and one looks for proof of conformance. As the part nonconformance statement is likely with unlimited statistical distributions in the inner and outer shells, assume unlimited distributions when estimating them. Adopting unlimited distribution, we always have $p'_c < 1$. This coheres with the proposed criterion for stating nonconformance $p'_c \geq 1 - \beta$, discouraging nonconformance statements.

4.2. Simulation based estimate of p'_c

Having estimated $f_{e,NSM}\left(GV_{i,j,k}\right)$, the exact evaluation of p'_c still needs a theoretical calculation of the probability in (30). This is difficult. However, an easier way is possible.

Considering the estimated $f_{e,NSM}\left(GV_{i,j,k}\right)$, simulating a single instance of all $GV_{i,j,k}$ in NSM is easy. And similarly it is possible to verify if the simulated NSM conforms to the volumetric tolerance. Performing n_{sim} simulation runs and with n_{conf} being the total number of simulations yielding a conformance statement, let's estimate p'_c as:

$$\hat{p}'_c = \frac{n_{conf}}{n_{sim}} \tag{34}$$

This is the value to use in the decision rule described in §4. Compared to the time required for scanning and reconstructing XCT images the time required for the simulation is negligible (few seconds).

5. Validation

To validate the proposed method, two case studies are proposed. The first one is based on an AM part, and aims at demonstrating the application of the

method. The second one considers a calibrated sample characterized by a simple geometry. The repeated measurements of this sample allows the verification of the predicted p'_c reliability.

5.1. AM part: application of the method

The first case study is a 20 mm high puppet made by selective laser melting of stainless steel powder, and in particular its head. The model of the puppet, in .stl format, is open-access on cults3d.com [40]. The reasons for this choice are as follows. First, the puppet head has an approximately spherical geometry, and this makes it easier to handle both manual and automatic alignment. Furthermore, the spherical geometry makes it easier to understand geometric errors like shape or size deviations. Finally, a limited number of triangles constitute the part, of course nominally planar. If in the future one would consider the nominal planar geometry of the triangles, this would be possible.

Applying the Matlab™ `inpolyhedron` function [41] yields the nominal voxel representation. This function verifies whether voxels at defined coordinates are inside or outside a mesh. The $NV_{i,j,k}$ value is set as:

$$NV_{i,j,k} = \begin{cases} 0, & \text{the voxel is inside the mesh} \\ 1, & \text{the voxel is outside the mesh} \end{cases} \tag{35}$$

Fig. 12 (left) shows the result of the application of (35).

A NSI X25 XCT scanner scanned the puppet applying the following scan parameters:

- Voltage: 140 kV
- Current: 47 mA
- Target power: 6.58 W
- Acquisition rate: 13.24 fps
- Number of projections: 600
- Filter: 2.5 mm stainless steel

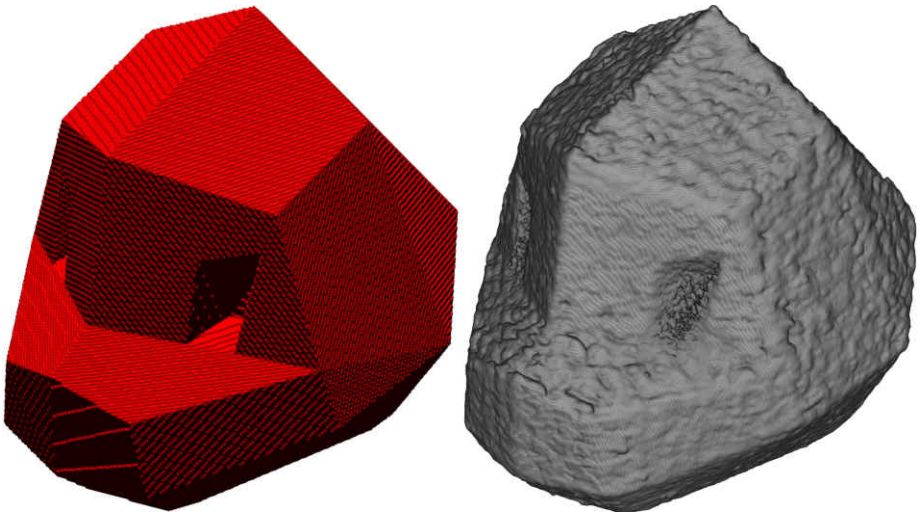

Figure 12: Voxel representation of the case study. On the left: nominal geometry; on the right: XCT image.

- Voxel size: 17.67 µm
- Image size: 508(x)x491(y)x439(z) voxels

Five scan replicas were taken. Fig. 12 (right) shows a typical XCT image of the puppet head.

Registering the nominal and scanned representations of the head make them occupy (approximately) the same portion of space. The nominal and measured representations are heterogeneous: the nominal representation is, according to (35), binary, while in the measured representation presents a full range of $GV_{i,j,k}$. Literature [42] suggests mutual information maximization as a criterion for registering heterogeneous representations.

The transition zone considers the nominal geometry of the part. If the desired transition zone amplitude is T, and $d_{i,j,k}$ is the signed distance of voxel i, j, k from the mesh (positive if the voxel is external to the mesh), define the

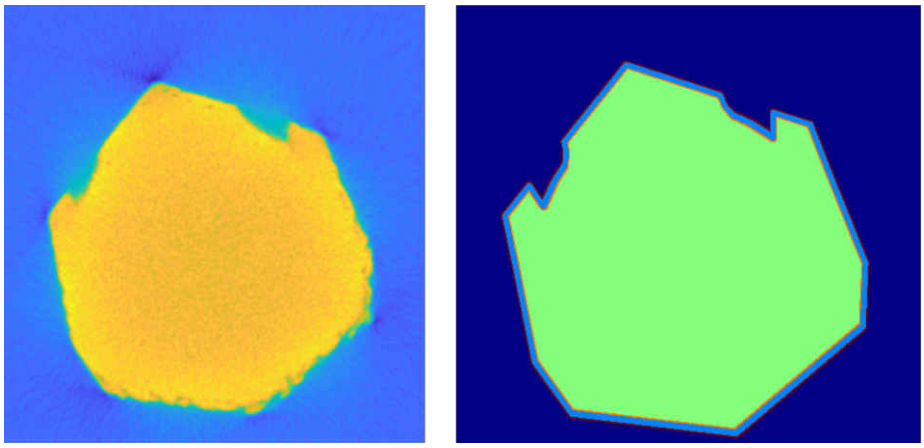

Figure 13: Slices in the measured image and the VMGTS. On the left: a measured slice. On the right: the corresponding slice in the VMGTS. Blue corresponds to air, red to the outer shell, azure to the transition zone, orange to the inner shell, and green to the material. In this example, $T = 0.1$ mm.

VMGT as:

$$tv_{i,j,k} = \begin{cases} m, & & & d_{i,j,k} & < & - & T/2 \\ t, & - & T/2 & \leq & d_{i,j,k} & \leq & T/2 \\ a, & & T/2 & < & d_{i,j,k} & & \end{cases} \tag{36}$$

This way of defining the transition zone is the closest to the conventional profile tolerance zone defined in the ISO 1101 standard [43]. Finally, the shells are computed as described in (2). Fig. 13 compares a measured slice to the corresponding slice from the VMGTS.

To perform the simulation, let's estimate the statistical distribution of the values in the shells using the method described in §4.1. In the kernel estimation set the three parameters: *(i)* the bandwidth of the kernel, *(ii)* the lower quantile defining the lower tail and *(iii)* the upper quantile defining the upper tail. As many points are available, use a small bandwidth to better approximate the density function. In this study a value equal to 0.5 % of the range of the measured gray values was used. To avoid the peaks close to the tails and have enough points to perform the MLE estimation, the values of the lower (q_l) and

upper (q_u) tail quantiles must be small enough. The proposed value of q_l is:

$$q_l = \max\left\{100, \left|\left\{\begin{array}{c} GV_{i,j,k} | GV_{i,j,k} \in NSM_I \vee GV_{i,j,k} < \\ < \max\left\{gv_{o,p,q} | gv_{o,p,q} \in NSM_O\right\} \end{array}\right\}\right|\right\}/n_i \quad (37)$$

In practice, choose q_l equal to the fraction of voxels in NSM_I showing a value lower than the maximum value found in NSM_O. To guarantee an adequate number of values to estimate the lower tail density at least 100 values concur to the tail distribution definition. Set the value of q_u as:

$$q_u = 1 - \max\left\{100, \left|\left\{\begin{array}{c} GV_{i,j,k} | GV_{i,j,k} \in NSM_O \vee GV_{i,j,k} > \\ > \min\left\{gv_{o,p,q} | gv_{o,p,q} \in NSM_I\right\} \end{array}\right\}\right|\right\}/n_o \quad (38)$$

Fig. 14 shows density and cumulative probability functions of the inner and outer shells for $T = 70$ µm.

Let's apply the proposed methodology to the five XCT images with varying values of T. The value of T is varied in the range $[0.02, 1]$ mm, in steps of 0.02 mm. Identifying $f_{e,NSM}\left(GV_{i,j,k}\right)$ for all different values of T made it possible to perform 1000 simulation runs at each different transition zone amplitude and for each XCT image. In each simulation run applying (34) yielded the estimate of $\hat{p'_c}$.

Fig. 15 summarizes the results of the simulation in a 95% interval plot of $\hat{p'_c}$ as the value of T varies. When T is small the conformance statement probability is equal to 0; instead, when the T is large the probability is equal to 1. A sharp transition from 0 to 1 is visible when the value of T is about 0.78 mm. This coheres with the NMI shown in Fig. 17, and indicates that the geometric deviation of the part should be approximately equal to this value. The curve zone where it moves from 0 to 1 is equivalent to an uncertainty zone [27]. Similarly, the area after the transition corresponds to an acceptance zone (when verifying conformity), and the area before to a rejection zone (when verifying nonconformity).

It is worth noting that the 95% confidence interval on p'_c when $T = 0.78$ mm is very wide. In fact, for $T = 0.78$ mm the values of $\hat{p'_c}$ calculated for the

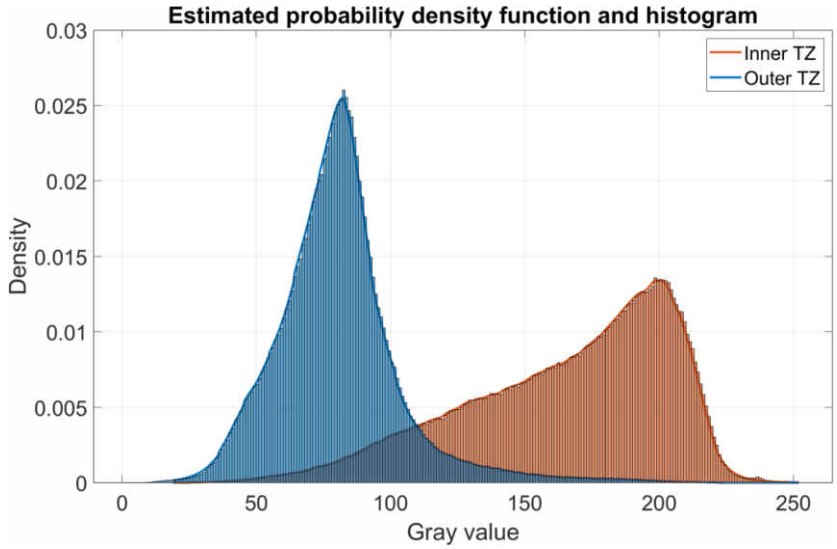

(a) Density distribution function

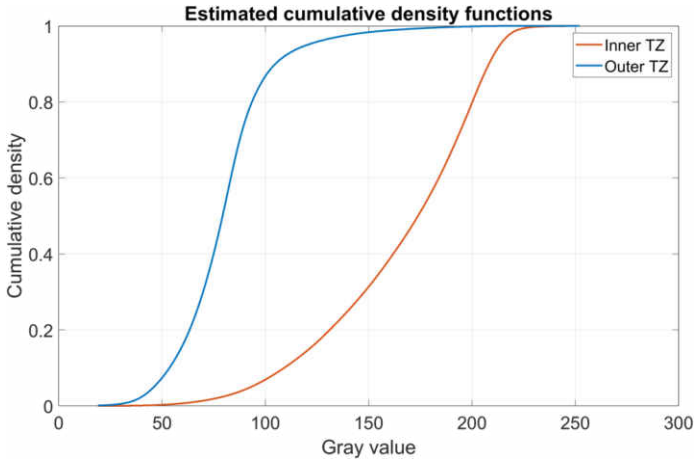

(b) Cumulative distribution function

Figure 14: Estimated density and cumulative distribution functions of the voxels in the inner and outer shells

five XCT images vary significantly. This is due to the measurement variability between the XCT images, combined with the fact that the amplitude of the transition zone is similar to the magnitude of the geometric deviation. Fig. 16 shows the histogram of $GV_{i,j,k}$ in the shells of a XCT image when $T = 0.78$

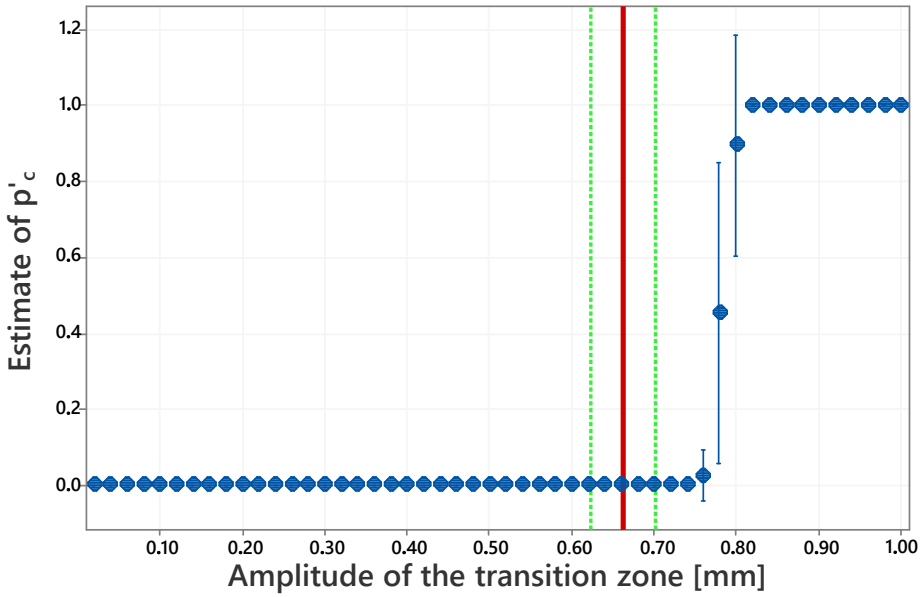

Figure 15: 95% interval plot of p'_c as the transition interval amplitude varies. The vertical red line indicates the estimated global profile deviation, and the green lines indicate the related coverage interval with a coverage factor equal to 2.

mm. It is apparent that the distribution of $GV_{i,j,k}$ in the outer shell presents an anomalous right tail. This is due to a portion of material out of the transition zone. Of course, if the transition zone is larger this portion of material would be found inside the transition zone and the right tail would disappear.

Fig. 17 plots a 95% interval plot of the normalized mutual information (NMI) [44] as the value of T varies for the five XCT images. Given two signals A and B, define the NMI as:

$$NMI\left(A,B\right)=\frac{I\left(A,B\right)}{\min\left\{H\left(A\right),H\left(B\right)\right\}} \tag{39}$$

As in our case $H\left(NSM\right)>H\left(NSN\right)$, $NMI\left(NSM,NSN\right)=I\left(NSM,NSN\right)/H\left(NSN\right)$. Therefore, (9) turns into $NMI\left(NSM,NSN\right)=1$. Fig. 17 shows that the NMI tends to 1 (the full separation of the shells) as the value of T increases. This was expected, as the increase of transition zone width makes fulfilling the geometric specification easier. Although the value 1 seems reached when T is

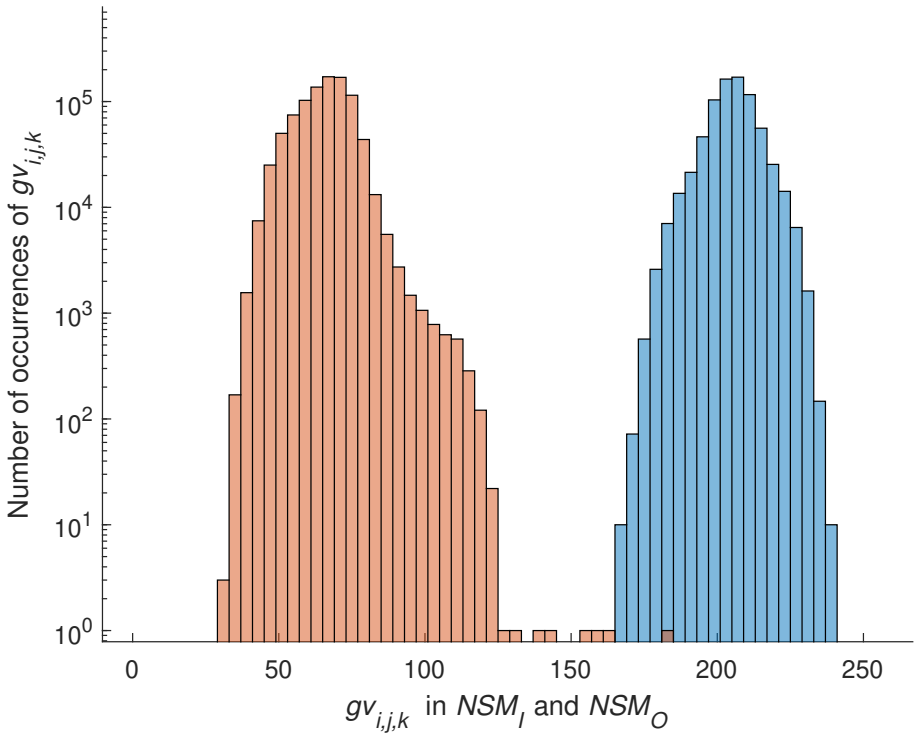

Figure 16: Histogram of the $GV_{i,j,k}$ in the inner and outer shells when $T = 0.78$ mm. The y-axis scale is logarithmic.

approximately equal to 0.3 mm, $NMI = 1$ only when $T \geq 0.8$ mm.

Let's compare the result obtained from the proposed approach to the conventional segmentation-comparison to the nominal geometry (profile) approach. A local version of the Chan and Vese algorithm [45] segmented the five XCT images. The iterative closest point algorithm [46] implemented in CloudCompare [47] aligned the resulting meshes to the nominal mesh. Deviations of every point from the original mesh are calculated (Fig. 18). Twice the maximum absolute local deviation is an estimate of the global geometric deviation of the segmented surface. On average, the global deviation is 0.66 mm, with a standard deviation of the mean equal to 0.02 mm. The latter is a rough type A estimate of the standard uncertainty. This value is lower than the obtained value of 0.78 mm for the transition (see Fig. 15). A couple of reasons can mo-

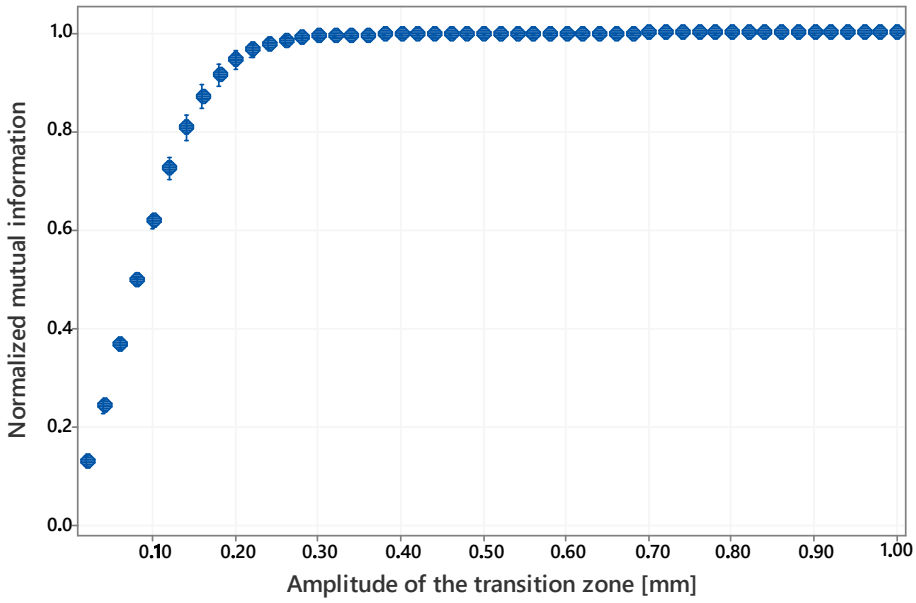

Figure 17: 95% interval plot of NMI as the transition interval amplitude varies.

tivate this. First, applying the Chan and Vese algorithm required denoising of the XCT image, which tended to smooth the image. Second, the segmentation tends to pass in the middle of the transition zone, identifying a middle point where the measured value gradient is maximum. The approach based on mutual information tends instead to consider the whole distribution until no ambiguity shows up between material and air. Therefore, the mutual information-based approach is more conservative in declaring a part to be conforming.

It is worth noting that the surface of the part is very rough, which is common in AM. The presence of roughness affects the measurement accuracy [48]. If the XCT scan resolution is low, the rough surface is seen as partially material-filled. This makes both the air/material boundary and the transition of p'_c from 0 to 1 less sharp. However, the presence of roughness is expected to similarly affect the conventional segmentation-based approach, and even a conventional coordinate measurement.

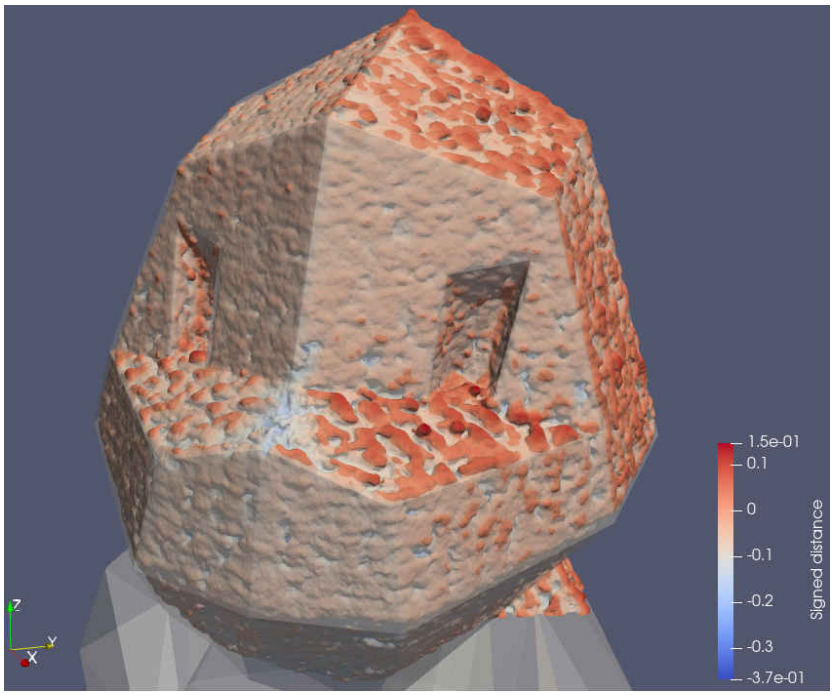

(a) Reconstructed mesh

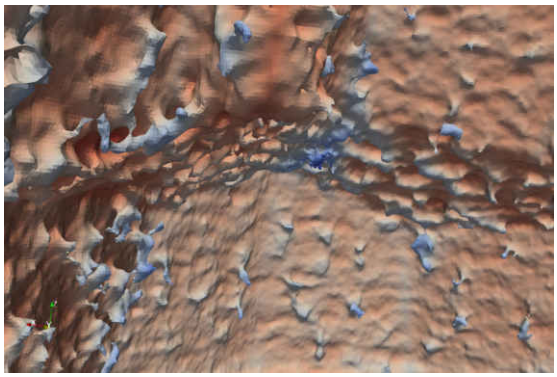

(b) Magnification of the reconstructed mesh

Figure 18: Segmented surface for one of the XCT volumes and signed distance between the measured mesh and the nominal geometry

5.2. Calibrated part: validation of the empirical distribution generation

To verify that the empirical distributions are correctly estimated, a multi-diameter Ti6Al4V – Grade 5 titanium alloy cylinder was used (Fig. 20) [32].

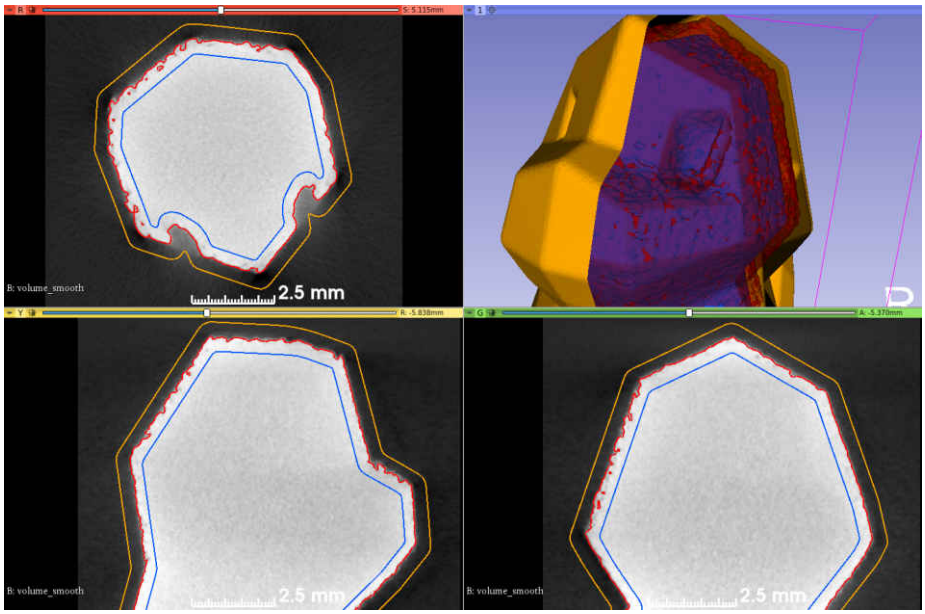

Figure 19: Measured XCT volume with reconstructed mesh (red), inner envelope (blue) and outer envelope (orange). The two envelopes are computed using a value of 0.39 mm

The sample design allowed five XCT images of a cylinder per each XCT scan. All the diameters were calibrated on a Zeiss Prismo VAST HTG coordinate measuring machine (Tab. 2).

Figure 20: Calibrated sample

The sample was scanned on a NSI X25 micro-focus XCT scanner. The scan

Nominal diameter [mm]	**Calibrated diameter [mm]**	**Calibrated cylindiricity deviation [mm]**	**Amplitude of the transition zone [mm]**
18	18.0584(2)	0.0101(3)	0.0535
15	15.0704(9)	0.0172(4)	0.0751
12	12.0707(2)	0.0133(8)	0.0269
9	9.0798(2)	0.033(3)	0.0251
6	6.0760(4)	0.0129(6)	0.0165

Table 2: Nominal diameter, calibrated diameter, calibrated cylindricity deviation and selected amplitude of the transition zone for each level of the calibrated sample. In parentheses the uncertainty is reported referring to the last decimal (where applicable).

parameters were changed in the various measurement repetitions. In particular, voltage and the presence or absence of a physical filter were considered. This allows to prove the robustness of the method when the measurement conditions change. In order to obtain good quality XCT scans, the X-Ray source current has been set depending on the combination of voltage and filter.

The chosen levels for the parameters were:

1. X-Ray source voltage
    - Low level: 100 kV (current: 98 µA with filter / 95 µA without filter)
    - High level: 160 kV (current: 45 µA with filter / 14 µA without filter)
2. Physical filter
    - Low level: no filter
    - High level: 0.5 mm Ti filter
3. Sample diameter
    - 6-9-12-15-18 mm

The experiment was repeated twice. In total, eight XCT scans were performed yielding forty cylinder measurements.

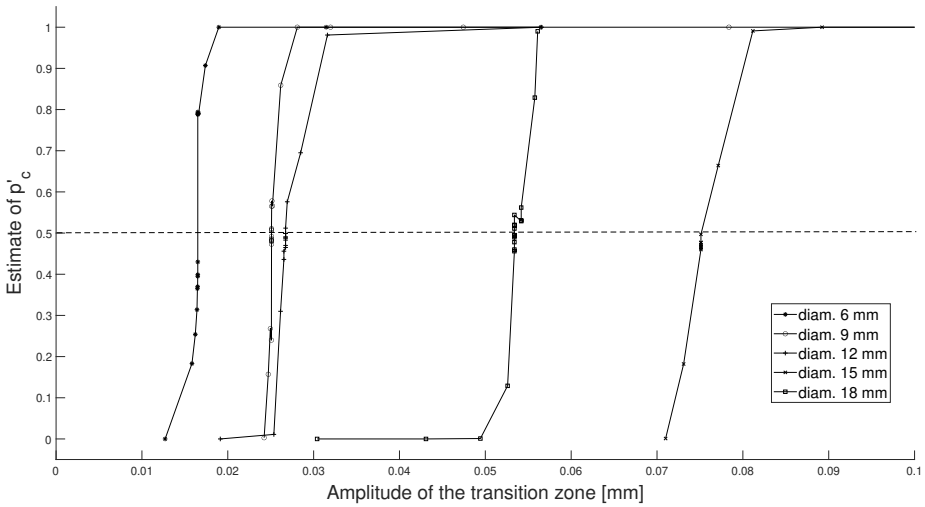

Figure 21: Identification of the amplitude of the transition zone for which $p'_c = 0.5$. As a search algorithm has been used, points tend to concentrate close to searched point.

The resulting XCT images where then separated in five parts, each one being the VRMO of a single level on the sample. Each level was separately registered to the volumetric representation of the nominal geometry, considering the calibrated calibrated diameter. Maximization of the mutual information was the registration criterion.

To study the behavior of the proposed approach, a simple VGMT has been built, that is the voxel representation of a perfect cylinder characterized by the calibrated diameter, around which a transition zone of defined amplitude has been added. The amplitude of the transition zone has been chosen in the following way. A VRMO from each level was randomly selected from the eight available images. The NSM were extracted from it and the empirical distribution was estimated as explained in §5.1. Now, suppose the amplitude of the transition zone is selected so that the $p'_c = 0.5$. This can be done selecting the correct point in an amplitude of the tolerance zone - p'_c plot (Fig. 21), or, preferably, by applying a search algorithm. Using this amplitude it is expected that condition (9) is satisfied twenty times in forty considered VRMO. The selected amplitudes are reported in Tab. 2. Condition (9) was finally applied to the

forty measurements, and was satisfied twenty-five times. Although this differs from the expected twenty successes, a statistical test proves that there is no statistical evidence to reject the hypothesis $p'_c = 0.5$ (p-value 0.154). This proves that our method correctly estimates p'_c, and that it is robust to the variation of the scan parameters (provided that the scan parameters are selected so that resulting quality of the XCT images is good).

Finally, the amplitudes of the tolerance zone for which $p'_c = 0.5$ can be considered a sort of estimate of the actual amplitude of the tolerance zone. Having a look to Fig. 15 and 21, it is evident that this value is located approximately between the amplitudes for which $p'_c = 0.05$ $p'_c = 0.95$ respectively. It is then the center of a sort of uncertainty range of the proposed criterion. Therefore, it is interesting to compare the calibrated cylindricity deviation at each level to it (Tab. 2). It is evident that the two values differ significantly, and in most cases the selected amplitude is larger than the cylindricity deviation. Surely this is in part due to the limited voxel size of the images (13.31 µm). In most cases this is of the same order of magnitude of the cylindricity deviation. The only exception to this is for ⌀9 mm, which also is the only case in which the amplitude of the transition zone is smaller than the cylindricity deviation. But also confirms that the proposed methodology verifies something different from the conventional coordinate metrology.

6. Conclusions and future aims

In this paper, a new tool for the volumetric verification of AM parts introduced in previous papers has been deepened. The tool is based on mutual information between a volumetric representation of the nominal part together with its tolerance and a measured volumetric representation of the real part. The tool particularly performs well if using volumetric design and representation on the part, and XCT is adopted for the verification. The new tool required introducing the concepts of maximum and minimum material continuum together with their volumetric representation.

The statistical basis of the method has been analyzed. This made possible to define consumer's and producer's risks, crucial when looking for reliable rules for stating conformance and nonconformance. Considering consumer's and producer's risks in the decision rules is analogous to the consideration of measurement uncertainty in the conventional context of measurement result-based rules. The absence of a measurement result in the proposed method made a risk-based approach necessary. A simulation-based approach to the actual evaluation of the risks has been proposed. It envisages an a-posteriori application, after the XCT image acquisition. No particular assumption on the measurement procedure was made, thus making it easy and almost supervision-free.

Finally, an AM and a calibrated case studies illustrated the method application. The method has shown consistent results. However, a comparison with the conventional approach of XCT image segmentation and comparison with nominal surface geometry has shown that the proposed approach is conservative when stating a part to be conforming. A deep comparison of the proposed and conventional approach is needed to understand the extent to which they are comparable and if they are verifying the same quality characteristic of the part.

This is, of course, open to further developments. Here are some suggestions.

First, only a-posteriori application is possible for the proposed method. Although this makes it inexpensive and easy to apply, it makes it inapplicable at the inspection design level. A method to estimate the risks a-priori is needed to design the inspection correctly.

Second, the proposed method implicitly assumes that VMGT and XCT images share the same size and voxel size. This is not always the case, due to the resolution limits of XCT and resolution needs of the VMGT. The method applicability study when the resolutions of VMGT and XCT image are different is of interest.

Third, the method is currently applied to the raw XCT image. Although this is the easiest way, the XCT image improves by applying techniques like filtering, denoising, and image enhancement. The impact of these techniques is

to be studied.

Fourth, roughness surely influences the verification result. A complete study of the impact of roughness on the method effectiveness is envisaged.

Fifth, the form discussed in this paper the method is applied in way similar to form tolerances in GD&T. In fact, the registration between the nominal volumetric model and the VRMO is not subject to any constraints. If conditions similar to related GD&T tolerances are of interest, the registration should be constrained (orientation) or completely defined by some datum features (location). How manage this situations is to be deepened.

Finally, even if the method has been proven effective, from an industrial point of view its application is difficult. The operator should accept the conformance/nonconformance verdict without really understanding how it has been obtained, as he has no control over the simulation. Although this resembles the application of a virtual coordinate measuring machine to estimate the uncertainty in conventional coordinate metrology, the subject is worth further investigation.

Acknowledgments

Financial support to this work was provided as part of the AMaLa – Advanced Manufacturing Laboratory project, funded by Politecnico di Milano (Italy), CUP: D46D13000540005.

The Italian Ministry of Education, University and Research is acknowledged for the support provided through the Project "Department of Excellence LIS4.0 - Lightweight and Smart Structures for Industry 4.0" (CUP: D56C18000400006).

The authors wish to thank Trumpf GMbH for providing the TruPrint 3000 system on which the AM part case study was printed, and Ms. Valentina Finazzi for her support in the printing process.

References

[1] G. Moroni, S. Petrò, W. Polini, Geometrical product specification and verification in additive manufacturing, CIRP Annals - Manufacturing Technology 66 (1) (2017) 157–160. doi:10.1016/j.cirp.2017.04.043.
URL https://linkinghub.elsevier.com/retrieve/pii/S0007850617300434

[2] M. K. Thompson, G. Moroni, T. Vaneker, G. Fadel, R. I. Campbell, I. Gibson, A. Bernard, J. Schulz, P. Graf, B. Ahuja, F. Martina, Design for Additive Manufacturing: Trends, opportunities, considerations, and constraints, CIRP Annals - Manufacturing Technology 65 (2) (2016) 737–760. doi:10.1016/j.cirp.2016.05.004.

[3] Vaneker, T. and Bernard, A. and Moroni, G. and Gibson, I. and Zhang, Y., Design for Additive Manufacturing: Framework and Methodology, CIRP Annals – Manufacturing Technology 69 (2), in press (2020).

[4] E. Morse, J.-Y. Dantan, N. Anwer, R. Söderberg, G. Moroni, A. Qureshi, X. Jiang, L. Mathieu, Tolerancing: Managing uncertainty from conceptual design to final product, CIRP Annals 67 (2) (2018) 695–717. doi:10.1016/j.cirp.2018.05.009.

[5] ZMorph, Voxelizer 3D (2016).
URL https://zmorph3d.com/products/voxelizer-software

[6] J. Plocher, A. Panesar, Review on design and structural optimisation in additive manufacturing: Towards next-generation lightweight structures, Materials and Design 183 (2019) 108164. doi:10.1016/j.matdes.2019.108164.

[7] T. Takahashi, A. Masumori, M. Fujii, H. Tanaka, FAV (Fabricatable Voxel) File Format Specification (2018).
URL https://www.fujixerox.com/eng/company/technology/communication/3d/fav.html

[8] J. P. Kruth, M. Bartscher, S. Carmignato, R. Schmitt, L. De Chiffre, A. Weckenmann, Computed tomography for dimensional metrology,

CIRP Annals - Manufacturing Technology 60 (2) (2011) 821–842. doi:10.1016/j.cirp.2011.05.006.

[9] L. De Chiffre, S. Carmignato, J.-P. Kruth, R. Schmitt, A. Weckenmann, Industrial applications of computed tomography, CIRP Annals - Manufacturing Technology 63 (2) (2014) 655–677. doi:10.1016/j.cirp.2014.05.011.

[10] A. Thompson, I. Maskery, R. K. Leach, X-ray computed tomography for additive manufacturing: a review, Measurement Science and Technology 27 (7) (2016) 72001. doi:10.1088/0957-0233/27/7/072001.

[11] S. Carmignato, W. Dewulf, R. Leach, Industrial X-ray computed tomography, 1st Edition, Springer International Publishing, Cham, Switzerland, 2017. doi:10.1007/978-3-319-59573-3.

[12] A. Townsend, R. Racasan, R. Leach, N. Senin, A. Thompson, A. Ramsey, D. Bate, P. Woolliams, S. Brown, L. Blunt, An interlaboratory comparison of X-ray computed tomography measurement for texture and dimensional characterisation of additively manufactured parts, Additive Manufacturing 23 (2018) 422–432. doi:10.1016/j.addma.2018.08.013.

[13] A. Du Plessis, I. Yadroitsev, I. Yadroitsava, S. G. Le Roux, X-Ray Microcomputed Tomography in Additive Manufacturing: A Review of the Current Technology and Applications, 3D Printing and Additive Manufacturing 5 (3) (2018) 227–247. doi:10.1089/3dp.2018.0060.

[14] A. du Plessis, S. G. le Roux, Standardized X-ray tomography testing of additively manufactured parts: A round robin test, Additive Manufacturing 24 (2018) 125–136. doi:10.1016/j.addma.2018.09.014.

[15] A. du Plessis, S. G. le Roux, J. Waller, P. Sperling, N. Achilles, A. Beerlink, J. F. Métayer, M. Sinico, G. Probst, W. Dewulf, F. Bittner, H. J. Endres, M. Willner, Á. Drégelyi-Kiss, T. Zikmund, J. Laznovsky, J. Kaiser, P. Pinter, S. Dietrich, E. Lopez, O. Fitzek, P. Konrad, Laboratory X-ray

tomography for metal additive manufacturing: Round robin test, Additive Manufacturing 30 (2019) 100837. doi:10.1016/j.addma.2019.100837.

[16] The Association of German Engineers, VDI/VDE 2630 Blatt 2.1: Computed tomography in dimensional measurement - Determination of the uncertainty of measurement and the test process suitability of coordinate measurement systems with CT sensors (2015).

[17] S. Carmignato, Accuracy of industrial computed tomography measurements: Experimental results from an international comparison, CIRP Annals - Manufacturing Technology 61 (1) (2012) 491–494. doi:10.1016/j.cirp.2012.03.021.

[18] J. Hiller, L. M. Reindl, A computer simulation platform for the estimation of measurement uncertainties in dimensional X-ray computed tomography, Measurement: Journal of the International Measurement Confederation 45 (8) (2012) 2166–2182. doi:10.1016/j.measurement.2012.05.030.

[19] J. Hiller, M. Maisl, L. M. Reindl, Physical characterization and performance evaluation of an x-ray micro-computed tomography system for dimensional metrology applications, Measurement Science & Technology 23 (8) (2012) 85404. doi:10.1088/0957-0233/23/8/085404.

[20] J. Hiller, G. Genta, G. Barbato, L. De Chiffre, R. Levi, Measurement uncertainty evaluation in dimensional X-ray computed tomography using the bootstrap method, International Journal of Precision Engineering and Manufacturing 15 (4) (2014) 617–622. doi:10.1007/s12541-014-0379-9.

[21] W. Dewulf, K. Kiekens, Y. Tan, F. Welkenhuyzen, J. P. Kruth, Uncertainty determination and quantification for dimensional measurements with industrial computed tomography, CIRP Annals - Manufacturing Technology 62 (1) (2013) 535–538. doi:10.1016/j.cirp.2013.03.017.

[22] P. Müller, J. Hiller, Y. Dai, J. L. Andreasen, H. N. Hansen, L. De Chiffre, Estimation of measurement uncertainties in X-ray computed

tomography metrology using the substitution method, CIRP Journal of Manufacturing Science and Technology 7 (3) (2014) 222–232. doi:10.1016/j.cirpj.2014.04.002.

[23] J. Angel, L. De Chiffre, Comparison on Computed Tomography using industrial items, CIRP Annals - Manufacturing Technology 63 (1) (2014) 473–476. doi:10.1016/j.cirp.2014.03.034.

[24] J. J. Lifton, A. A. Malcolm, J. W. McBride, On the uncertainty of surface determination in x-ray computed tomography for dimensional metrology, Meas. Sci. Techn. 26 (3) (2015). doi:10.1088/0957-0233/26/3/035003.

[25] R. Jimenez, M. Torralba, J. A. Yague-Fabra, S. Ontiveros, G. Tosello, Experimental Approach for the Uncertainty Assessment of 3D Complex Geometry Dimensional Measurements Using Computed Tomography at the mm and Sub-mm Scales, Sensors 17 (5) (2017) E1137.

[26] Joint Committee for Guides in Metrology, ISO/IEC GUIDE 98-4: Uncertainty of measurement - Part 4: Role of measurement uncertainty in conformity assessment (2012).

[27] International Organization for Standardization, ISO 14253-1: Geometrical Product Specifications (GPS) - Geometrical product specifications (GPS) - Inspection by measurement of workpieces and measuring equipment - Part 1: Decision rules for proving conformance or nonconformance with specifications (2017).

[28] J. A. Yagüe-Fabra, S. Ontiveros, R. Jiménez, S. Chitchian, G. Tosello, S. Carmignato, A 3D edge detection technique for surface extraction in computed tomography for dimensional metrology applications, CIRP Annals - Manufacturing Technology 62 (1) (2013) 531–534. doi:10.1016/j.cirp.2013.03.016.

[29] G. Moroni, S. Petrò, Impact of the Threshold on the Performance Verifi-

cation of Computerized Tomography Scanners, Procedia CIRP 43 (2016) 345–350. doi:10.1016/j.procir.2016.02.082.

[30] F. Borges de Oliveira, A. Stolfi, M. Bartscher, L. De Chiffre, U. Neuschaefer-Rube, Experimental investigation of surface determination process on multi-material components for dimensional computed tomography, Case Stud. Nondestruct. Test. Eval. 6 (2016) 93–103. doi:10.1016/j.csndt.2016.04.003.

[31] G. Moroni, S. Petrò, A discussion on performance verification of 3D X-ray computed tomography systems, Procedia CIRP 75 (2018) 125–130. doi:10.1016/j.procir.2018.04.064.

[32] G. Moroni, S. Petrò, An experimental study on segmentation in X-Ray Computed Tomography, in: The E-Journal Of nondestructive Testing, Vol. 24, 2019, pp. 1–7.
URL http://www.ndt.net/?id=23731

[33] G. Moroni, S. Petrò, Segmentation-free geometrical verification of additively manufactured components by x-ray computed tomography, CIRP Annals - Manufacturing Technology 67 (1) (2018) 519–522. doi:10.1016/j.cirp.2018.04.011.

[34] T. M. Cover, J. A. Thomas, Differential Entropy, in: Elements of Information Theory, Wiley, 2005, pp. 243–259. doi:10.1002/047174882x.ch8.

[35] T. M. Cover, J. A. Thomas, Entropy, Relative Entropy, and Mutual Information, in: Elements of Information Theory, 2nd Edition, Wiley, 2005, Ch. 2, pp. 13–55. doi:10.1002/047174882X.ch2.

[36] E. Parzen, On estimation of a probability density function and mode, Ann. Math. Statist. 33 (3) (1962) 1065–1076. doi:10.1214/aoms/1177704472.
URL https://doi.org/10.1214/aoms/1177704472

[37] B. W. Silverman, Monographs on statistics and applied probability, Density estimation for statistics and data analysis 26 (1986).

[38] The Mathworks, Inc., Natick, Massachusetts, MATLAB (R2019b) (2019).

[39] R. A. Johnson, D. W. Wichern, et al., Applied multivariate statistical analysis, Vol. 5, Prentice hall Upper Saddle River, NJ, 2002.

[40] A. Flowalistik, Low-Poly Charmander (2020).
URL https://cults3d.com/en/3d-model/game/low-poly-charmander

[41] S. Holcomb, inpolyhedron - are points inside a triangulated volume? (2012).
URL https://it.mathworks.com/matlabcentral/fileexchange/37856-inpolyhedron-are-points-i

[42] J. Pluim, J. Maintz, M. Viergever, Mutual-information-based registration of medical images: a survey, IEEE Transactions on Medical Imaging 22 (8) (2003) 986–1004. doi:10.1109/TMI.2003.815867.

[43] International Organization for Standardization, ISO 1101: Geometrical product specifications (GPS) - Geometrical tolerancing - Tolerances of form, orientation, location and run-out (2017).

[44] Y. Y. Yao, Information-Theoretic Measures for Knowledge Discovery and Data Mining, Vol. 119 of Studies in Fuzziness and Soft Computing, Springer Berlin Heidelberg, Berlin, Germany, 2003, Ch. 6, pp. 115–136. doi:10.1007/978-3-540-36212-8_6.

[45] W. Li, C. Lu, J. Zhang, Review of vision real-time inspection algorithm for rolling steel surface defects, Advances in Materials Research 308-310 (2011) 1328–1332. doi:10.4028/www.scientific.net/AMR.308-310.1328.

[46] P. Besl, N. D. McKay, A method for registration of 3-D shapes, IEEE Transactions on Pattern Analysis and Machine Intelligence 14 (2) (1992) 239–256. doi:10.1109/34.121791.

[47] CloudCompare, Cloudcompare (version 2.9) [gpl software] (2018).
URL http://www.cloudcompare.org/

[48] A. Townsend, L. Pagani, L. Blunt, P. J. Scott, X. Jiang, Factors affecting the accuracy of areal surface texture data extraction from X-ray

CT, CIRP Annals - Manufacturing Technology 66 (1) (2017) 547–550. doi:10.1016/j.cirp.2017.04.074.